Ulm University Hospital

Clinic for Internal Medicine II

Medical director: Prof. Dr. W. Rottbauer

Age- and Gender-related Reference Values of Biventricular Strains measured by Cardiovascular Magnetic Resonance Based Tissue Tracking

DISSERTATION

Dissertation submitted for Doctor Degree of Medicine (Dr. Med.)

Faculty of Medicine, Ulm University

Submitted by

Yangyang Qu

Born in Yancheng, Jiangsu, P. R. China

2019

Amtierender Dekan: Prof. Dr. rer. nat. ThomasWirth

1. Berichterstatter: Prof. Dr. rer. nat. Volker Rasche

2. Berichterstatter: Prof. Dr. med. Meinrad Beer

Tag der Promotion: 29-07-2021

Part of this dissertation has already been published in the following peer-reviewed papers:

1. **Yang-Yang Qu**, Hao Li, Wolfgang Rottbauer, Gen-Shan Ma, Dominik Buckert, Volker Rasche. Right ventricular free wall longitudinal strain and strain rate quantification with cardiovascular magnetic resonance based tissue tracking. International Journal of Cardiovascular Imaging. 2020 Oct;36(10):1985-1996. doi: 10.1007/s10554-020-01895-5.

   Distributed under CC BY 4.0, http://creativecommons.org/licenses/by/4.0/

2. **Yang-Yang Qu**, Jan Paul, Hao Li, Gen-Shan Ma, Dominik Buckert, Volker Rasche. Left ventricular myocardial strain quantification with two- and three-dimensional cardiovascular magnetic resonance based tissue tracking. Quantitative Imaging in Medicine and Surgery. 2021 Apr;11(4):1421-1436. doi: 10.21037/qims-20-635.

   Distributed under CC BY-NC-ND 4.0, https://creativecommons.org/licenses/by-nc-nd/4.0/

Both articles are distributed under creative commons licenses. All rights remain with the authors.

Contents

Contents I

Abbreviations III

1 Introduction 1

1.1 Cardiovascular magnetic resonance 1

1.2 Myocardial structure and deformation 2

1.3 Myocardial strain 6

1.3.1 Definition and computation 6

1.3.2 Potential clinical applications 8

1.3.3 Imaging modalities used for strain assessment 10

1.3.3.1 Tissue Doppler imaging 10

1.3.3.2 Speckle tracking echocardiography 11

1.3.3.3 CMR tissue tagging 12

1.3.3.4 CMR based feature tracking and tissue tracking 13

1.4 Aim of this dissertation 15

2 Materials and Methods 16

2.1 Materials 16

2.1.1 Study subjects 16

2.1.2 CVI[42] software package 17

2.2 Methods 19

2.2.1 Image acquisition 19

2.2.2 Clinical data collections 19

2.2.3 CMR-TT operation: two- or three-dimension (2/3D) 21

2.2.4 Statistical analysis 25

3 Results 27

3.1 Characteristics of the study participants 27

3.1.1 Demography of the subjects 27

3.1.2 LV morphology and function 28

3.1.3 RV morphology and function 29
3.2 LV strain measurement 30
3.2.1 LV segmental strains 30
3.2.1.1 Feasibility of LV segmental strain measurement 30
3.2.1.2 Reference values of LV segmental strains 34
3.2.2 LV regional strains 39
3.2.3 LV global strains 41
3.2.3.1 Reference values of LV 2/3D global strains 41
3.2.3.2 Gender- and age-related difference of 3D global peak strains 45
3.2.3.3 Correlation analysis of 3D global peak strains 47
3.2.4 Reproducibility of LV 2/3D CMR-TT 49
3.3 RVFW strain measurement 52
3.3.1 RVFW global, regional and segmental longitudinal peak strains 52
3.3.2 Gender- and age-related differences of RVFW-GLS 53
3.3.3 Gender- and age-related differences of RVFW-RLS and SLS 55
3.3.4 Correlation analysis of RVFW-GLS_{myo} 56
4 Discussion 57
4.1 The measurement of LV and RV strains using CMR-TT technique 57
4.2 Feasibility and reproducibility of 2/3D CMR-TT on LV strain measurement 60
4.3 Reference values of RV strains 62
4.4 Gender- and age-related difference of LV and RV global peak strains 64
4.5 Limitations of this study 66
5 Summary 68
6 Reference 70
7 Acknowledgement 81
8 Curriculum vitae 83

Abbreviations

^{1}H	Hydrogen atom
2D	Two-dimensional
3D	Three-dimensional
AHA	American Heart Association
ANOVA	Analysis of variance
AS	Ascending segment
AUC	Area under the curve
BMI	Body mass index
BSA	Body surface area
CI	Cardiac index / Confidence interval
CMR	Cardiovascular magnetic resonance
CMR-FT	Cardiovascular magnetic resonance based feature tracking
CMR-TT	Cardiovascular magnetic resonance based tissue tracking
CO	Cardiac output
CoV	Coefficient of variation
CS	Circumferential strain
CSPAMM	Complementary spatial modulation of magnetization
DBP	Diastolic blood pressure
DS	Descending segment
EF	Ejection fraction

eGFR	Estimated glomerular filtration rate
GCS	Global circumferential peak strain
GLS	Global longitudinal peak strain
GLS_{endo}	Global longitudinal peak strain of endocardium
GLS_{epi}	Global longitudinal peak strain of epicardium
GLS_{myo}	Global longitudinal peak strain of myocardium
GRS	Global radial peak strain
HR	Heart rate
HVMB	Helical ventricular myocardial band
ICC	Intra-class correlation coefficient
LAX	Long-axis
LS	Left segment / Longitudinal strain
LV	Left ventricle / Left-ventricular
LVEDV(I)	Left-ventricular end-diastolic volume (index)
LVESV(I)	Left-ventricular end-systolic volume (index)
LVMM	Left-ventricular myocardial mass
LVSV(I)	Left-ventricular stroke volume (index)
M(D)	Mean (difference)
MCS	Global circumferential mean strain
MLS	Global longitudinal mean strain
MRS	Global radial mean strain
r	Correlation coefficient

RCS	Regional circumferencial strain
RLS	Regional longitudinal strain
RRS	Regional radial strain
RS	Right segment / Radial strain
RV	Right ventricle / Right-ventricular
RVEDV(I)	Right-ventricular end-diastolic volume (index)
RVESV(I)	Right-ventricular end-systolic volume (index)
RVFW	Right-ventricular free wall
RVSV(I)	Right-ventricular stroke volume (index)
SAX	Short-axis
SBP	Systolic blood pressure
SCS	Segmental circumferential peak strain
SD	Standard deviation
SLS	Segmental longitudinal peak strain
SPAMM	Spatial modulation of magnetization
SRS	Segmental radial peak strain
SSFP	Steady-state in free-precession
STE	Speckle tracking echocardiography
TDI	Tissue Doppler imaging

1 Introduction

1.1 Cardiovascular magnetic resonance

Cardiovascular magnetic resonance (CMR) is a non-invasive medical imaging technique to assess the morphological and functional features of the cardiovascular system in a highly reproducible manner (American College of Cardiology Foundation Task Force on Expert Consensus et al. 2010; Lamacie et al. 2017; Petersen et al. 2017). It works on the basis of nuclear magnetic resonance, which is associated with the selective absorption of radiofrequency energy of atomic nuclei and its re-emission (Pennell et al. 2004). Even though several nuclei with an odd number of protons and neutrons exist in organs and tissues, the hydrogen atom (^{1}H) is regarded as the principal option for clinical imaging because of its high occurrence in biological tissue (Mitchell et al. 2016). Upon patients entering into a scanner with a strong magnetic field strengths (ranging from 0.15 to 7 tesla), hydrogen nuclei create a net tissue magnetization aligned with the direction of the axis of the magnetic field (Plewes and Kucharczyk 2012; Ridgway 2010). After so-called excitation of the spins, the magnetic resonance signal can be measured by external receive coils.

CMR plays a fundamental role in measuring comprehensive tissue characterization, including myocardial perfusion, edema and fibrosis. Due to its high spatial and temporal resolution, good soft tissue contrast and high coverage without exposure to ionizing radiation and iodinated intravenous contrast medium, it has become the gold standard for diagnosis and subsequent monitoring of cardiovascular diseases (Pennell et al. 2004; von Knobelsdorff-Brenkenhoff and Schulz-Menger 2016).

1.2 Myocardial structure and deformation

The theory of helical ventricular myocardial band (HVMB, Figure 1) that was proposed by a Spanish scientist named Francisco Torrent Guasp (1931–2005) on the basis of dissection in 1972 provided a new insight into the global, three-dimensional (3D) and functional architecture of the ventricular myocardium (Kocica et al. 2006; Kocica et al. 2007). He proposed that the biventricular myocardium is a single muscular band that consists of a 3D double-loop helicoid, of which one is the basal loop (from the root of the pulmonary artery to the beginning of the central fold) and the other one is the apical loop (from the beginning of the central fold to the root of the aorta). Each of the loop is comprised of two segments. The left and right segment which coincide with the left- and right-ventricular (LV and RV) free wall constitute the basal loop. The apical loop is divided into ascending (AS) and descending (DS) segments. After the 180° twist at the central fold of the HVMB, the descendant fibers make a 90° turn around the apex and become the ascendant fibers (Kocica et al. 2007; Torrent-Guasp et al. 2001). It is likely that the helical anatomic configuration of HVMB dictates the ventricular performance. The extension of HVMB from pulmonary artery to the aorta and activation from the base to apex help explain the complex mechanical phenomenon revealed in CMR studies: (i) a downward movement of the ventricular base towards the apex during systolic phases; (ii) a continuous clockwise rotation of the apex and a change from initially clockwise to finally counterclockwise rotation at the basal part during systolic contraction; and (iii) the opposite movement during diastole (Ballester-Rodes et al. 2005; Kocica et al. 2007).

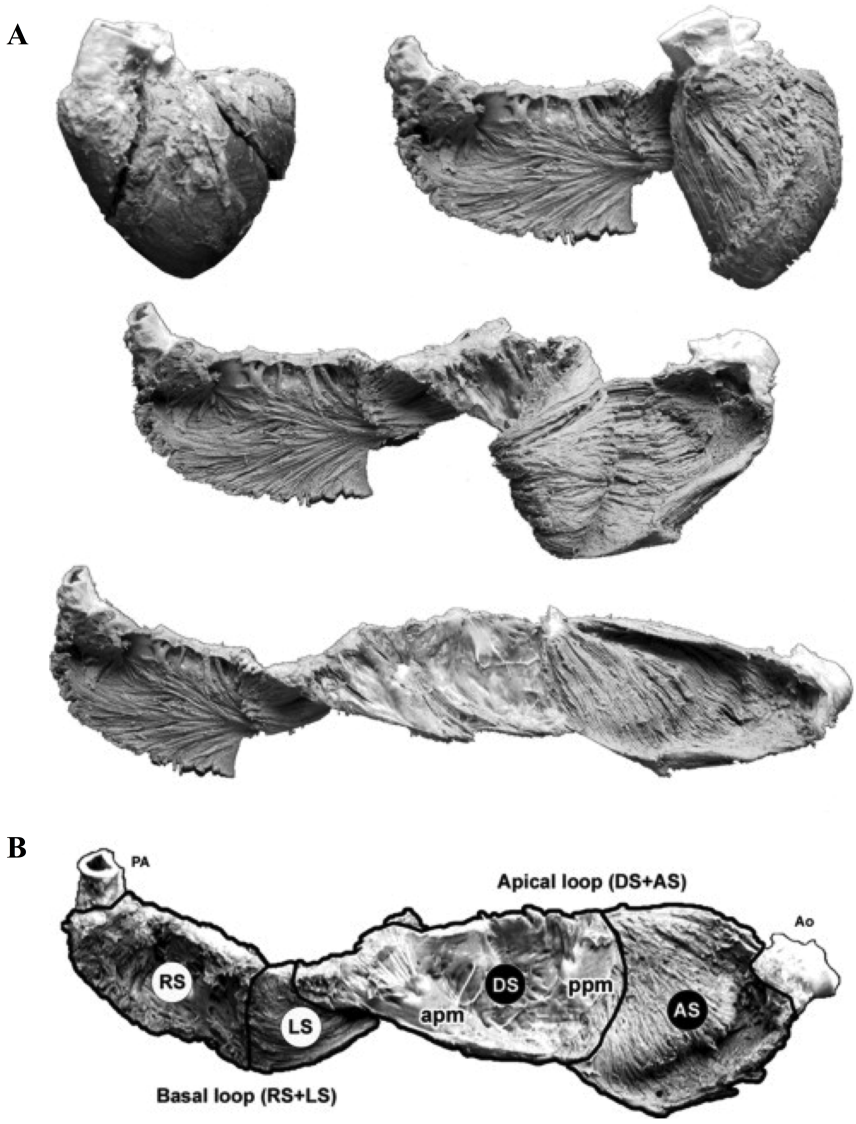


Figure 1. The anatomic configuration of helical ventricular myocardial band (HVMB). (A) Five main successive stages of the bovine HVMB dissection. (B) HVMB consists of a basal (from the root of the pulmonary artery to the beginning of the central fold) and apical (from the beginning of the central fold to the root of the aorta) loop. The posterior interventricular sulcus divides the basal loop into left (LS) and right segment (RS). The apical loop is divided into ascending (AS) and descending (DS) segments. apm, anterior papillary muscle; ppm, posterior papillary muscle; PA, pulmonary artery; Ao, aorta (Kocica et al. 2007), reprinted with kind permission from Elsevier.

The myocardium is a transmural continuum between two helical fiber geometries, one is a sub-endocardial right-handed helix and the other one is a sub-epicardial left-handed helix (Sengupta et al. 2006). LV myocardial cross-sectional view in the short-axis (SAX) plane

discovered the longitudinal myofiber orientation in the sub-endocardium, transverse or circumferential fiber orientation in the mid-myocardium, and oblique myofiber orientation in the sub-epicardium (Luis et al. 2019). The contraction of inner sub-endocardial fibers rotates the apex clockwise and the base counterclockwise, while contraction of outer sub-epicardial fibers rotate the apex and base in exactly the opposite directions. Because of the larger radius of epicardium compared with endocardium, the epicardium dominates LV overall rotation (Omar et al. 2015). Streeter et al introduced the helix and transverse angles for quantifying fiber orientation (Streeter et al. 1969). The myofiber helix angle is the angle between the circumferential axis and the projection of the myofiber onto the circumferential-longitudinal plane. It typically changes from +60° at the sub-endocardium to −60° at the sub-epicardium, continuously. The transverse angle is the angle between the circumferential axis and the projection of myofiber orientation onto the radial-circumferential plane and ranges between −20° to +20° (Sengupta et al. 2006). This orthogonal fiber orientation results in the opposite directions of rotation at LV base and apex as well as a “wringing-like” cardiac emptying effect during systole (Luis et al. 2019) .

The complex anatomic structure of myocardial fiber bundles in the bi-ventricles determines the mechanic and deformation of heart. During systole, the contraction of the heart starts from RV free wall (RVFW), then contraction of the LV free wall take place. Consequently, the entire basal loop becomes a stiff external cylinder. Subsequent contraction of the DS pulls the ventricular base to move towards the apex on the purpose of shortening the ventricular long axis, reducing the chamber volume and allowing ventricular ejection. The

ultimate contraction of the AS causes the increase of longitudinal length of the ventricle and an upward movement of the basal part against the apex, then ventricular cavity expands and fills with blood (Ballester-Rodes et al. 2005; Torrent-Guasp et al. 2001). This unique anatomic and spatial configuration of the myocardial fibers causes ventricular ejection and relaxation.

1.3 Myocardial strain

1.3.1 Definition and computation

Myocardial strain is defined as the percentage change of myocardial fiber length compared with the initial state (usually end diastole) in a certain direction. It can be expressed either as a decimal fraction such as 0.20 or as a percentage such as 20% (Abraham et al. 2007; Pedrizzetti et al. 2016). Strain can be expressed either in a local cardiac coordinate system or in a fiber coordinate system. The local cardiac coordinate system is defined by three perpendicular axes orienting the geometry of the LV as radial, circumferential and longitudinal directions. The establishment of local fiber coordinate system is a bit more complex than the local cardiac coordinate system as the following: (a) the radial axis--similar to the local cardiac coordinate system; (b) the fiber axis--tangent to the surface and parallel to the local fiber orientation; (c) the cross-fiber axis: tangent to the surface and perpendicular to the fiber (Sengupta et al. 2006).

Myocardial strain enables the description of change of the thickness and length (L) of myocardial fibers and implies the dynamic thinning or thickening as well as shortening or lengthening deformation of myocardial wall with respect to an initial end-diastolic length L_0. There're two kinds of strains, Lagrangian strain referring to an initially undeformed state, and Eulerian strain that normalizes the difference in lengths with the ultimate length L rather than L_0. Lagrangian strain is more widely used and generates lower absolute values in practice (Abraham et al. 2007; Amzulescu et al. 2019). Based on this, Lagrangian strain is defined as: $\text{Strain} = (L - L_0)/L_0$.

Strain is a vector with distinctly spatial orientations of myocardial contraction resulted from the 3D double-helix arrangement of myocardium. According to the different directions in which the myocardium deforms, radial, circumferential and longitudinal strain (RS, CS and LS) can be calculated (Figure 2). RS suggests the radially directed myocardial deformation towards the center of the ventricular chamber, and indicates the thinning and thickening of the wall. CS is measured as the change in length of myocardial fiber along the circular boundary on the short-axis cine images. LS shows the longitudinal deformation of myocardial fibers from the base to the apex (Scatteia et al. 2017). In practice, SAX cine images were tracked to generate RS and CS, while long-axis (LAX) cine images were used to generate RS and LS. The radial contraction and thickening of myocardial wall towards the center results in positive RS. The clockwise motion of the myocardial fibers at base and counterclockwise rotation at apex as seen from apex to base cause the "wringing motion" and reduce the ventricular cavity size at systole. This process also known as circumferential shortening resulted in a negative CS. The longitudinal movement of ventricular base towards apex, resulting in myocardial shortening, is denoted by negative LS (Abraham et al. 2007; Pedrizzetti et al. 2016). In case of the confusion caused by the expression of positive or negative values, strain can also be expressed as absolute values or placed in square brackets.

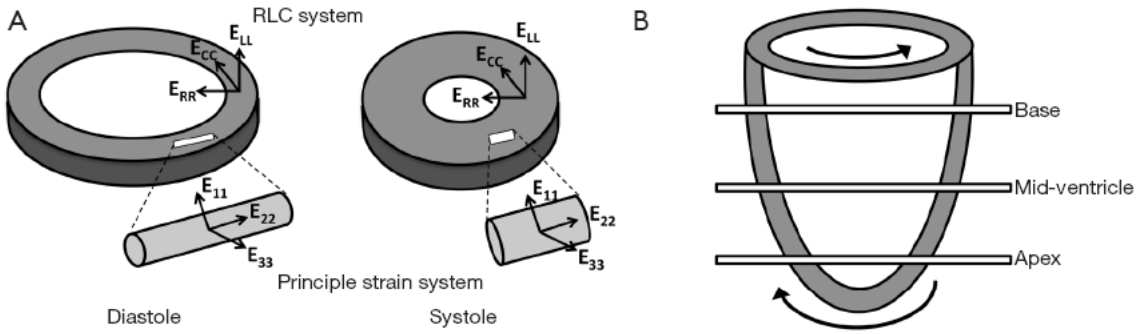


Figure 2. Left-ventricular (LV) myocardial deformation during contraction. (A) Myocardial wall strains in Radial-Circumferential-Longitudinal. The radial strain (E_{RR}), circumferential strain (E_{CC}), and longitudinal strain (E_{LL}) were defined to describe the LV wall thickening in the radial direction and shortening in the circumferential and longitudinal directions, respectively. (B) As seen from apex to base, the LV apical wall twists counterclockwise and the base wall twists clockwise during contraction (Jiang and Yu 2014), reprinted with kind permission from AME.

1.3.2 Potential clinical applications

Recently, myocardial strain has proven promising in assessing myocardial contraction. Traditionally, in routine clinical practice using either CMR or echocardiography, ejection fraction (EF) is widely used as a parameter to assess ventricular global function and exerted great values in diagnosis and prognosis among patients with cardiovascular diseases. There is a correlation between global systolic peak strain and the EF. For example, Taylor et al reported that LV global RS (GRS) was modestly correlated with LVEF (correlation coefficient [r]=0.63, P<0.001) (Taylor et al. 2015). Kawakubo et al revealed that negative correlations existed not only between LV global LS (GLS) and LVEF (r=-0.71, P<0.01) but also between RV GLS and RVEF (r=-0.35, P<0.01) (Kawakubo et al. 2016). However, EF cannot assess the regional variation of myocardial dysfunction and only provides limited information on myocardial mechanical activity (Abraham et al. 2007; Amzulescu et al. 2019). It has been shown that the deterioration in global systolic function as detected by EF occurs

later than the onset of cardiac pathology. Here, strain may play a more sensitive role in detecting subclinical and subtle ventricular dysfunction and predicting prognosis. Hence, myocardial strain has raised the physicians and researchers' attention in clinical routine as well as in research (Lamacie et al. 2017; Taylor et al. 2015).

Myocardial strain plays an essential role in detecting abnormality of myocardial function in a variety of diseases, such as bicuspid aortic valve disease, cardiomyopathy, acute myocarditis and heart failure with preserved EF (Claus et al. 2015; Luetkens et al. 2018; Maceira et al. 2018; Nucifora et al. 2018). Riffel et al found that the transmural LS played a better role in discriminating healthy volunteers and patients than EF since the area under the curve (AUC) were 0.94 and 0.84, respectively (Riffel et al. 2015). CMR-derived strains may reveal subtle impairment in biventricular mechanical activity among heart failure patients, even though the EF is normal for some patients (Zou et al. 2018). A systematic review and meta-analysis of prospective randomized studies proposed that GLS had a moderately accurate value for differentiating myocardial infarction size >12% and <12% (Diao et al. 2017). The regional strain could also identify the infarcted segments and correlated with the extent of transmural infarction (Weidemann et al. 2006).

Myocardial strain is able to provide strong prognostic information for various kinds of patients. Patients with GLS higher than −15.1% demonstrated hazard ratio of 4.5 (95% confidence interval [CI] 2.1–9.7) for all-cause mortality (Antoni et al. 2010). Stress GLS was significantly related with risk of major adverse cardiac events, and patients with stress GLS ≥-19% had significantly lower event-free survival compared with those with stress

GLS < -19% (log-rank *P*< 0.001) (Romano et al. 2019). RVFW-GLS was reported not only to be an independent predictor of cardiac events among patients with acute decompensated heart failure but also play a more powerful role in predicting prognosis than RV traditional parameters (Hamada-Harimura et al. 2018).

1.3.3 Imaging modalities used for strain assessment

The surgically implanted radiopaque markers in canine hearts were tracked with X-ray imaging for the quantitative measurement of ventricular wall motion. However, the process is invasive and can't be used into humans. Furthermore, the invasive implantation can affect the regional even global myocardial deformation during the tracking process and hence limits its application in the clinical routine and research environment (Wazen et al. 2013). By comparison, the promising and noninvasive imaging techniques are thriving and clinically feasible (Wang and Amini 2012).

1.3.3.1 Tissue Doppler imaging

The application of tissue Doppler imaging (TDI) has been introduced to measure the motion of both mitral and tricuspid annuli, and to assess LV and RV systolic function. The important parameter produced by TDI is velocity that can be assessed using color Doppler or pulsed Doppler mode and be post-processed for calculating global and segmental displacement, strain and strain rate (Opdahl et al. 2015; Pellerin et al. 2003). However, as a Doppler-based technique, the angle dependency of the ultrasound beam and its susceptibility to signal noise limit the number of myocardial segments that can be interrogated and its wide application in clinical routine (Luis et al. 2019). When myocardial segments move beyond the line of

ensonifying beam, inaccurate results can be generated. Besides, long analysis time and its considerable intra-observer and inter-observer variability in strain and strain rate measurement are two relevant weaknesses of TDI and limit its sensitivity and specificity in detecting functional and mechanical abnormalities (Abraham et al. 2007; Pislaru and Pellikka 2005).

1.3.3.2 Speckle tracking echocardiography

The speckle tracking echocardiography (STE) is a development in echocardiographic strain imaging. This technique works on the basis of tracking the motion of myocardial speckles generated by the interaction of ultrasound waves within the myocardium from frame to frame throughout the cardiac cycle. The motion of speckles is then integrated to produce a dimensional index of change in a particular direction. Finally, the whole cardiac chamber as well as the individual regions within cardiac chamber can be described in terms of radial thickening, circumferential rotation and longitudinal shortening (Luis et al. 2019).

Two-dimensional STE (2D-STE) tracks the movements of the myocardial natural acoustic markers or speckles from one frame to another on the basis of high-resolution frame rate imaging at 2D level. The semi-automated tracking of serial speckles allows the assessment of myocardial deformation within the plane and offers an easier, faster and less angle-dependent measurement of strain compared with TDI (Opdahl et al. 2015). While the accurate measurement of 2D-STE relies on high-resolution image quality and is susceptible to tachycardia, which consequently limits the widespread application of this modality in the clinical routine (Abraham et al. 2007).

3D-STE acquiring the 3D full-volume echocardiographic rendition of the ventricles from the apical window is a novel echocardiographic modality. It overcomes the limitation of plane dependency present in 2D-STE and be validated against sonomicrometry and CMR . It can track motion of speckles within the scan volume, irrespective of its direction (Opdahl et al. 2015). The regional strain measured with 3D STE may be revealed as color codes overlaid on the wall, and strain-time curves can be presented for all regions. However, 3D-STE is highly dependent on vendors and imaging quality, it is still not widely available.

1.3.3.3 CMR tissue tagging

CMR tissue tagging has become the gold standard for the assessment of myocardial deformation in research. This technique was initially introduced by Zerhouni and Axel et al (Axel and Dougherty 1989; Zerhouni et al. 1988). It uses a particular pulse sequence to spatially modulate the longitudinal magnetization prior to the conventional image acquisition, which alternates the light and dark patterns on the image. The measurement of myocardial deformation is based on the utilization of spin tagging pre-pulses to generate noninvasive markers in the myocardial patterns that persist during the systole. However, the tags may fade because of T1 relaxation of the magnetization, and higher field strength (>1.5 Testa) contributes to maintaining the tagging patterns (Wang and Amini 2012). Spatial modulation of magnetization (SPAMM) and complementary SPAMM (CSPAMM), which optimize tagging and acquisition of CMR images and have the advantage of longer net tag persistence by suppressing untagged blood, are utilized to produce tags (Axel and Dougherty 1989; Fischer et al. 1993). After the image acquisition and tag productions, the detection of

tag features and measurement of myocardial deformation used for quantitative analysis can be completed with the assistant of a variety of fast and accurate analysis methods (Wang and Amini 2012). These techniques have been endorsed for the measurement of global and regional wall motion in practice. However, due to the complexity of myocardial tagging acquisition and its indispensable post-processing analysis, CMR tissue tagging is only commonly used in the research environment rather than in clinical routine (Taylor et al. 2015).

1.3.3.4 CMR based feature tracking and tissue tracking

CMR based feature tracking (CMR-FT) and tissue tracking (CMR-TT) are two novel imaging approaches. They allow the quantitative assessment of wall motion and generate global and regional strain and strain rate throughout the whole cardiac cycle with a standard steady-state in free-precession (SSFP) sequence, which may facilitate the wide application in clinical routine (Hor et al. 2011).

The CMR-FT technique provided by TomTec software package (Unterschleissheim, Germany) tracks endo- and epicardial tissue (usually at basal, middle and apical slice). The technique we used in this study is CMR-TT provided by CVI[42] software package (Circle, Calgary, Canada), which can achieve both of 2D and 3D tracking of pixels/voxels placed on the myocardial borders and within the myocardium. So far, only few studies compared the values derived from FT and TT and their reproducibility. It was reported that strains measured by FT and TT were moderately to strongly correlated with LVEF and RVEF, and no significant correlation was found between RVFW-GLS and RVEF with either method.

CS generated by TT was lower than that by FT (Lu et al. 2019; Schuster et al. 2015). A better reproducibility for CS assessed with FT and lower variability for RS measured with TT were also reported (Schuster et al. 2015).

1.4 Aim of this dissertation

Up to date, the assessment of myocardial strain is based on echocardiography and CMR. The specific characteristics of these two methods and other software-related factors (such as type of strains, algorithms used for computation, and so on) cause high variability of the reported strains among the different studies.

In this study, we aimed to investigate the feasibility and reproducibility of CMR-TT in the measurement of LV and RV global, regional and segmental strain, and establish the normal reference values for LV and RV wall deformation. For LV assessment, resulting global, regional and modified American Heart Association (AHA) 16-segment strains and intra-observer reproducibility of 2D and 3D modes were assessed, and gender- and age-related difference as well as the correlation relationship of biventricular global strains were investigated.

2 Materials and Methods

2.1 Materials

2.1.1 Study subjects

To investigate the normal reference values of strain, 150 healthy volunteers undergoing CMR examination at Ulm University Medical Center were retrospectively recruited by the end of August 2016 for this study. The inclusion criteria were: above 18 years old, LVEF ≥ 55%, RVEF ≥ 40% and without history of cardiovascular diseases (Figure 3). Exclusion criteria were: pulmonary dysfunction, diabetes mellitus or impaired glucose tolerance, severe renal impairment (estimated glomerular filtration rate, eGFR < 30mL/min), metallic transplant or foreign matter, claustrophobia and pregnancy.

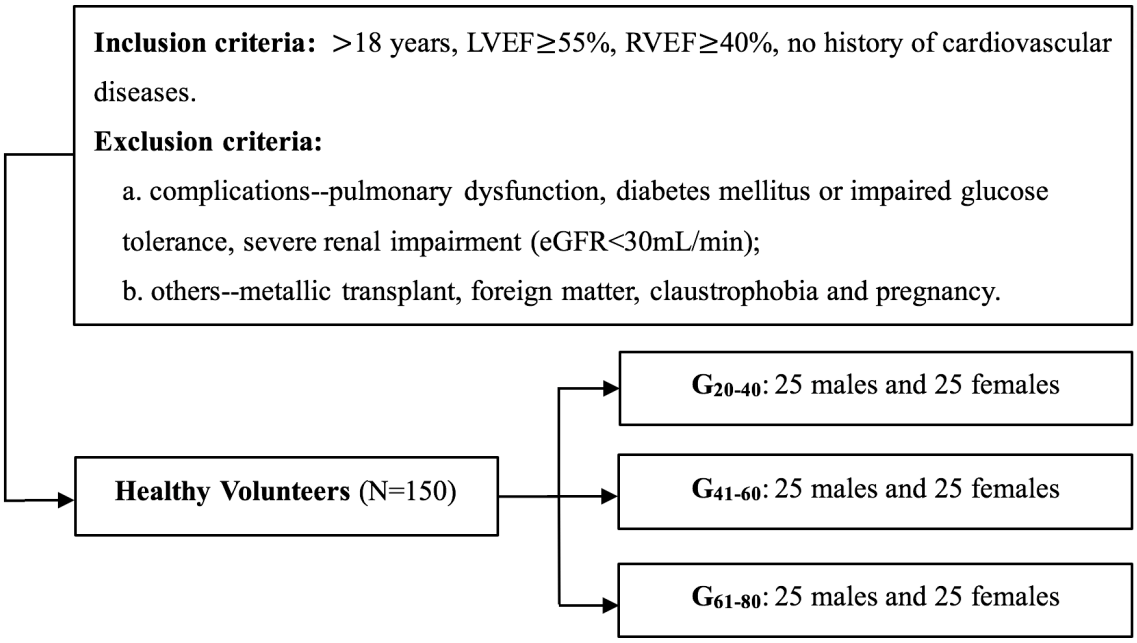


Figure 3. The protocol of recruiting study subject and setting subgroups. eGFR, estimated glomerular filtration rate.

Considering the potential existence of gender- and age-related difference of strain, subgroups were set according to gender and age. In practice, 150 healthy volunteers (75

males and 75 females) were equally divided into three age subgroups as $G_{20\text{-}40}$ (range 20-40 years, mean age 29.5±6.5 years), $G_{41\text{-}60}$ (range 41-60 years, mean age 51.0±6.0 years), and $G_{61\text{-}80}$ (range 61-80 years, mean age 69.1±5.8 years).

The study was approved by the local ethics committee. All subjects provided written informed consent.

2.1.2 CVI[42] software package

The post-processing software package used to perform CMR-TT in this study is CVI [42] (Circle, Calgary, Canada). Its mechanism is based on tracking myocardial features throughout the whole cardiac cycle with the assistance of a series of specific algorithms (Pedrizzetti et al. 2016). It was initially designed for LV tracking at 2D and 3D levels. Then with the development of CMR-TT technique and more attention paid on RV, CVI[42] also has been utilized to assess RV deformation at 2D level.

The methods used by LV 2D and 3D CMR-TT differ and have been reported by Circle and Liu et al before (Liu et al. 2018c). Briefly, 2D CMR-TT is based on a 2D algorithm and determines myocardial deformation by a series of reference points located on the myocardial wall in individual SAX or LAX cine images. These reference points can be automatically generated when the operator delineates the LV endo- and epi-cardial boundaries in a reference frame (usually at end diastole). With the contraction and relaxation of the myocardium, the positions of these reference points in each phase can be traced according to the tracked feature patterns and the incompressibility constraint of the model in two directions. 3D CMR-TT constructs a 3D deformation model by interpolating the tracked

borders from the 2D SAX and LAX images. The deformation of the 3D model is measured by tracking the positions of the reference points placed on myocardium in a reference phase (usually at end diastole) as in the case of 2D model. Finally, the myocardial motion can be quantitatively assessed in radial, circumferential and longitudinal directions together over the whole cardiac cycle.

It needs to be noticed that if only a stack of SAX images are used for tracking, the software can only enable 2D tracking and assess LV radial and circumferential deformation. Similarly, if only LAX images are used for tracking, the software merely performs 2D tracking and evaluates LV radial and longitudinal deformation. When both of SAX and LAX images ($n \geq 2$) are included, the software can perform 3D tracking. The more LAX images included for tracking, the more reliable 3D model is. LV 3D tracking costs more time than 2D tracking due to a load of semi-automatic delineation of endocardial and epicardial borders and more complex computational construction of the 3D model. Finally, the results of radial, circumferential and longitudinal mechanical parameters, like displacement, velocity, strain, strain rate and rotation are exported. Furthermore, the results can be displayed as time-strain curves and bull's eye patterns.

2.2 Methods

2.2.1 Image acquisition

All participants underwent CMR examination on a clinical 1.5 Tesla whole body scanner (Achieva, Philips Medical Systems, Best, The Netherlands) in supine position. The CMR scanner was equipped with a cardiac 32-channel phased-array receive coil. The CMR cine images acquired for the following analysis include 2-, 3-, and 4-chamber LAX view and an SAX stack covering the whole LV from base to apex. Data were acquired with an electrocardiogram-gated SSFP sequence. Typical scan parameters were as: echo time TE = 1.5ms, spatial resolution Δr = 1.7mm×1.7mm, repetition time TR = 3.0ms, field of view fov = 360mm×325mm, slice thickness s_D = 8mm, flip angle $\propto$ = 55°, slice gap Δs = 0mm.

2.2.2 Clinical data collections

Demographic, morphological and functional parameters were measured and recorded. Demographic parameters include: gender, age, height, weight, body mass index (BMI), body surface area (BSA), HR, systolic and diastolic blood pressure (SBP and DBP). Biventricular conventional morphological and functional analysis of the CMR cine data was performed by two experienced physicians with the standard commercial software provided by the vendor (ViewForum®, Philips Medical System, Best, The Netherlands). Analysis was performed as recommended by the Society for Cardiovascular Magnetic Resonance in 2013 (Schulz-Menger et al. 2013). End-diastolic and end-systolic phases were identified according to the change of LV dynamic volume throughout SAX cine images. Then, endocardium and epicardium were delineated semi-automatically at these two phases.

Papillary muscles were excluded from LV myocardial mass (LVMM). LV myocardial mass/end-diastolic volume (LVMM/LVEDV), end-diastolic and end-systolic volume (LVEDV and LVESV), end-diastolic and end-systolic volume index (LVEDVI and LVESVI), stroke volume (LVSV) and its index (LVSVI), cardiac output (CO), cardiac index (CI) and LVEF were measured. RV end-diastolic and end-systolic volume (RVEDV and RVESV), end-diastolic and end-systolic volume index (RVEDVI and RVESVI), stroke volume (RVSV) and its index (RVSVI) and RVEF were also measured. All of the indexed parameters were normalized by BSA. Finally, images were exported to an external workstation for subsequent CMR-TT offline analysis.

The categories and calculation formula of demographic, morphological and functional parameters are summarized as below:

(1) Demographic parameters: gender, age, height, weight, BMI, BSA, HR, SBP, DBP.

BMI (kg/m^2) =weight (kg) / $height^2$ (m)

BSA (m^2) =0.007184 × $height^{0.725}$ (cm) × $weight^{0.425}$ (kg)

(2) Morphological and functional parameters of LV: LVMM, LVMM/EDV, LVEDV, LVEDVI, LVESV, LVESVI, LVSV, LVSVI, CO, CI, LVEF.

LVMM (g) =1.05 (g/mL) × myocardial volume (mL)

LVEDVI (mL/m^2) =LVEDV (mL) / BSA (m^2)

LVESVI (mL/m^2) =LVESV (mL) / BSA (m^2)

LVSV (mL) =LVEDV (mL) - LVESV (mL)

LVSVI (mL/m^2) =[LVEDV (mL) - LVESV (mL)] / BSA (m^2)

CO (L/min) = LVSV (mL) × HR (bpm) / 1000

CI (L/min/m^2) =CO (L/min/) / BSA (m^2)

LVEF (%) = LVSV (mL) / LVEDV (mL)

(3) Morphological and functional parameters of RV: RVEDV, RVESV, RVEDVI, RVESVI, RVSV, RVSVI, RVEF.

RVEDVI (mL/m^2) =LVEDV (mL) / BSA (m^2)

RVESVI (mL/m^2) =LVESV (mL) / BSA (m^2)

RVSV (mL) =LVEDV (mL) - LVESV (mL)

RVSVI (mL/m^2) = [LVEDV (mL) - LVESV (mL)] / BSA (m^2)

RVEF (%) = RVSV (mL) / RVEDV (mL)

2.2.3 CMR-TT operation: two- or three-dimension (2/3D)

A SAX stack and 2-, 3-, and 4-chamber view LAX cine images were imported to the post-processing software CVI[42] (version 5.3.8) for the subsequent offline analysis. A well-trained operator, blinded to the group, performed the delineation of LV and RVFW endocardium and epicardium according to the procedure described in detail by the vendor. First, the LV and RV endocardium and epicardium were drawn semi-automatically at end diastole where the LV blood volume got maximal at the mid-ventricular level. Secondly, reference points of interventricular septum at SAX images and the line connecting the middle of mitral / tricuspid valve plane and apex were manually marked at the LAX images to facilitate the division of myocardial segments and quantification of the ventricular length. Thirdly, automatic tracking of the myocardium was performed through all cardiac phases using a

template matching algorithm. Manual corrections needed to be performed on the contours in case of failed border detection during the tracking (Figure 4**)**. Finally, LV 2D (separate analysis of SAX and LAX slices) and 3D (combined analysis of SAX and LAX slices [n≥2 for LAX]) assessment of global and segmental radial, circumferential and longitudinal systolic peak strain (GRS, GCS and GLS and SRS, SCS and SLS) as well as 2D RVFW-SLS were derived throughout the whole cardiac cycle.

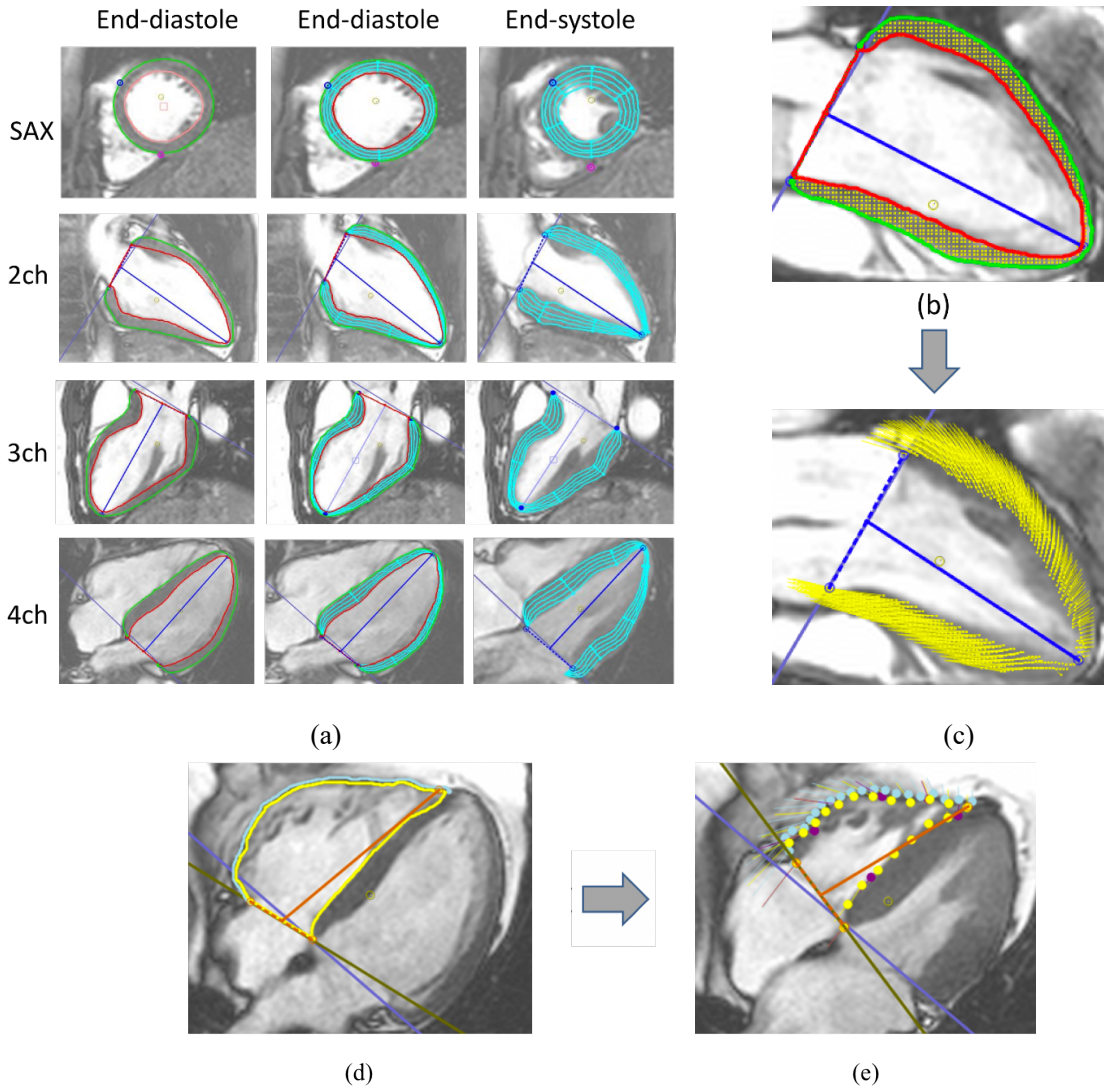


Figure 4 The operation of cardiovascular magnetic resonance based tissue tracking (CMR-TT). (a) Draw the left-ventricular (LV) endocardial and epicardial contours at end diastole; manually identify the reference points of interventricular septum and mitral valve plane, and finally start tracking with CVI[42]. The blue lines covering the whole myocardium were shown. (b-c) The yellow lines illustrate the movement of myocardial pixels at end systole compared to end diastole. (d-e) Draw the right-ventricular free wall (RVFW) endocardial and epicardial contours at end diastole, manually identify the reference points of tricuspid valve plane and then start tracking from the phase of end diastole. The round points represent the dynamic positions of endocardium and epicardium. A to c (Qu et al., 2021) CC BY-NC-ND 4.0, https://creativecommons.org/licenses/by-nc-nd/4.0/, d to e (Qu et al., 2020) CC BY 4.0, http://creativecommons.org/licenses/by/4.0/.

In this study, LV 2/3D global and segmental systolic peak strains and RV 2D segmental longitudinal systolic peak strains were derived by CVI[42] directly. 2/3D regional systolic radial, circumferential and longitudinal peak strains (RRS, RCS, RLS) were manually calculated by averaging two, four or six segmental strains in the corresponding area, as applicable. LV 2/3D global systolic radial, circumferential and longitudinal mean strains (MRS, MCS and MLS) were manually calculated by averaging all segmental systolic peak strain values. Similarly, RVFW-GLS was calculated by averaging all RVFW-SLS.

According to AHA 17-segment model (Cerqueira et al. 2002), sixteen segments analyzed for LV wall motion in this study are as listed: 1. basal anterior, 2. basal anteroseptal, 3. basal inferorseptal, 4. basal inferior, 5. basal inferolateral, 6. basal anterolateral, 7. mid anterior, 8. mid anteroseptal, 9. mid inferoseptal, 10. mid inferior, 11. mid inferolateral, 12. mid anterolateral, 13. apical anterior, 14. apical septal, 15. apical inferior, 16. apical lateral (Figure 5).

Considering that 2D CMR-TT could not perform tracking at all segments, the number and percentage of tracked segments featured with available data were recorded in order to evaluate the feasibility of both modalities. It should be noted that, in the context of 2D CMR-TT, SCS was derived from SAX and SLS was derived from LAX cine images, while SRS was derived from both SAX and LAX cine images. So the mean value of SRS from both of SAX and LAX was calculated for the following analysis. In some cases, SRS could merely be obtained from SAX or LAX cine images, then that value would be used for analysis.

The variability of strains was performed within 20 randomly selected subjects to reflect the intra-observer reproducibility of the measurement.

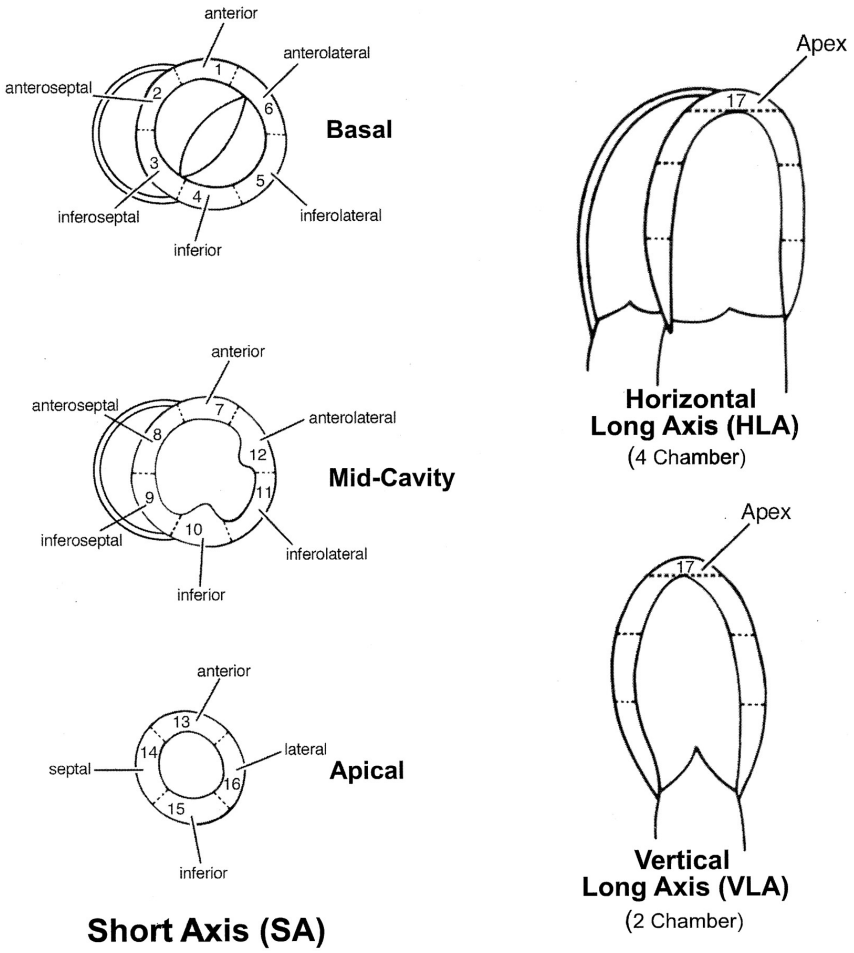


Figure 5. American Heart Association (AHA) 17-segment model. Diagram of short-axis (SAX) and 2-, 4-chamber view long-axis (LAX) image showing the number, name, location and anatomic landmarks for the selection of the basal (tips of the mitral valve leaflets), mid-cavity (papillary muscles), and apical (beyond papillary muscles but before cavity ends) SAX slices for the recommended 17-segment system (Cerqueira et al. 2002), reprinted with kind permission from Springer.

2.2.4 Statistical analysis

Numerical variables were described as mean ± standard deviation (M ± SD). Normal distribution of the data was tested using Shapiro-Wilk test. Depending on the distribution, differences between two groups were tested either by unpaired Student's t-test (data in normal distribution) or Mann-Whitney U test (data in skewed distribution). The comparisons

between 2D and 3D data were performed with paired Student's t-test or Wilcoxon's sign rank test, as appropriate. Age-related differences among three groups were evaluated with analysis of variance (ANOVA) or Kruskal-Wallis test followed by Bonferroni correction, as applicable. Correlation of strains was measured by Pearson correlation coefficient or Spearman's rank correlation coefficient (r), as appropriate. The intra-observer reproducibility was evaluated with intra-class correlation coefficient (ICC) and coefficient of variation (CoV). The reproducibility was considered excellent when ICC>0.74, good when ICC between 0.60 to 0.74, and fair when ICC between 0.40 to 0.59, and weak when ICC<0.40. CoV was defined as the SD of the differences divided by the mean. Statistical analysis was conducted using Excel (version 15.26, Microsoft, Redmond, Washington) and IBM SPSS (version 24, IBM, Armonk, New York). In all cases, two-tailed tests were applied and significance was determined as $P<0.05$.

3 Results

3.1 Characteristics of the study participants

3.1.1 Demography of the subjects

The demographic features of the investigated healthy volunteers are presented in Table 1. The whole study participants were 49.8±17.3 years old (range 20-80 years old). Compared with healthy females, males showed larger magnitude of height, weight and BSA (P<0.05). Age, BMI, HR, SBP and DBP were comparable between male and female groups (P >0.05).

Table 1: Demography of the study participants.

	Total (n=150)	Male (n=75)	Female (n=75)	P value
Age (yrs)	49.8 ± 17.3	49.9 ± 17.3	49.8 ± 17.5	0.984
Height (cm)	172.8 ± 9.5	179.2 ± 7.7	166.5 ± 6.3	**<0.001***
Weight (kg)	76.9 ± 15.5	82.4 ± 13.5	71.4 ± 15.5	**<0.001***
BSA (m^2)	1.9 ± 0.2	2.0 ± 0.2	1.8 ± 0.2	**<0.001***
BMI (kg/m^2)	25.7 ± 4.9	25.6 ± 3.8	25.8 ± 5.9	0.340
HR (bpm)	69.2 ± 14.7	68.0 ± 16.7	70.4 ± 12.4	0.087
SBP (mmHg)	121.5 ± 20.2	123.7 ± 13.8	120.8 ± 21.6	0.302
DBP (mmHg)	66.7 ± 11.1	69.0 ± 11.4	65.3 ± 8.5	0.106

Results are reported as mean ± standard deviation. *P<0.05: males vs. females.

Abbreviations: BSA, body surface area; BMI, body mass index; HR, heart rate; SBP, systolic blood pressure; DBP, diastolic blood pressure. (Qu et al., 2021) CC BY-NC-ND 4.0, https://creativecommons.org/licenses/by-nc-nd/4.0/

3.1.2 LV morphology and function

Table 2 summarizes the LV morphological and functional parameters of the investigated healthy volunteers. Compared with healthy females, males presented larger morphological magnitude, including LVMMI, LVMM/EDV, LVEDVI, LVESVI and LVSVI (P <0.05). There was no significant difference of LVCI and LVEF between male and female groups (*P*>0.05).

Table 2: LV morphological and functional parameters of the study participants.

	Total (n=150)	Male (n=75)	Female (n=75)	*P* value
LVMMI (g/m^2)	48.8±7.6	53.1±6.1	44.5±6.5	**<0.001***
LVMM/EDV (g/mL)	0.66±0.10	0.69±0.11	0.64±0.09	**0.001***
LVEDVI (mL/m^2)	74.6±12.9	78.7±13.5	70.5±10.8	**<0.001***
LVESVI (mL/m^2)	25.7±7.5	27.5±7.7	23.9±6.9	**0.002***
LVSVI (mL/m^2)	48.9±7.4	51.2±7.9	46.6±6.2	**<0.001***
LVCI (L/min/m^2)	3.4±0.8	3.4±0.9	3.3±0.7	0.278
LVEF (%)	66.0±5.8	65.4±5.5	66.6±6.0	0.161

Results are reported as mean ± standard deviation. **P*<0.05: males vs. females.

Abbreviations: LVMMI, left-ventricular myocardial mass index; LVMM/EDV, left-ventricular myocardial mass/end-diastolic volume; LVEDVI, left-ventricular end-diastolic volume index; LVESVI, left-ventricular end-systolic volume index; LVSVI, left-ventricular stroke volume index; LVCI, left-ventricular cardiac index; LVEF, left-ventricular ejection fraction. (Qu et al., 2021) CC BY-NC-ND 4.0, https://creativecommons.org/licenses/by-nc-nd/4.0/

3.1.3 RV morphology and function

Table 3 summarizes the RV morphological and functional parameters of the investigated healthy volunteers. Males presented significantly larger RVEDVI, RVESVI and RVSVI, and lower RVEF (60.8±6.9% vs. 65.5±6.6%) than females (P<0.05).

Table 3: RV morphological and functional parameters of the study participants.

	Total (n=150)	Male (n=75)	Female (n=75)	*P* value
RVEDVI (mL/m^2)	77.7±15.8	83.6±15.8	71.8±13.6	**<0.001***
RVESVI (mL/m^2)	29.7±9.7	33.7±10.0	25.8±7.6	**<0.001***
RVSVI (mL/m^2)	48.4±8.1	50.2±8.4	46.5±7.4	**0.005***
RVEF (%)	63.2±7.2	60.8±6.9	65.5±6.6	**<0.001***

Results are reported as mean ± standard deviation. *P<0.05: males vs. females.

Abbreviations: RVEDVI, right-ventricular end-diastolic volume index; RVESVI, right-ventricular end-systolic volume index; RVSVI, right-ventricular stroke volume index; RVEF, right-ventricular ejection fraction. (Qu et al., 2020) CC BY 4.0, http://creativecommons.org/licenses/by/4.0/

3.2 LV strain measurement

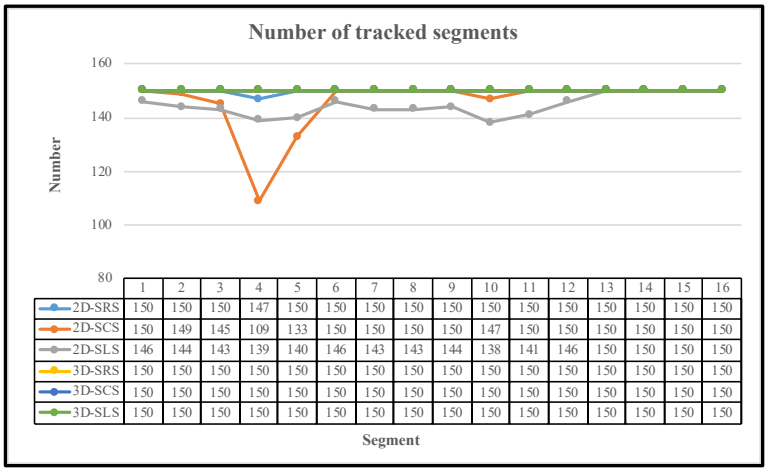
3.2.1 LV segmental strains

3.2.1.1 Feasibility of LV segmental strain measurement

Unsuccessfully tracked and measured segments (indicated with “nein” in the exported data) were excluded from analysis. The numbers of segments with strain data for 2D and 3D CMR-TT were recorded as N_{2D} and N_{3D}, the detailed information is presented in Figure 6 and Table 4-5.

With the utilization of 2D CMR-TT algorithms, only 97.3% (in SAX) and 96.4% (in LAX) segments were successfully measured in the radial direction. After combing the SRS generated from SAX and LAX together, 99.9% segments were quantitatively computed and used for the following analysis. Meanwhile, 97.3% segments from SAX and 96.4% segments from LAX cine images were assigned with RS and LS, respectively. By comparison, all segments could be tracked by 3D CMR-TT.

In the setting of 2D CMR-TT, we found that the proportion of successfully tracked SAX segments in the radial and circumferential directions was minimal in the basal part, especially at the basal inferior (72.7%). The proportion of successfully tracked LAX segments in the radial and longitudinal directions ranged from 92.0% to 100%. In the apical area, 100% segments were tracked and quantitatively measured with both of 2D and 3D CMR-TT.



	1	2	3	4	5	6	7	8	9	10	11	12	13	14	15	16
2D-SRS	150	150	150	147	150	150	150	150	150	150	150	150	150	150	150	150
2D-SCS	150	149	145	109	133	150	150	150	150	147	150	150	150	150	150	150
2D-SLS	146	144	143	139	140	146	143	143	144	138	141	146	150	150	150	150
3D-SRS	150	150	150	150	150	150	150	150	150	150	150	150	150	150	150	150
3D-SCS	150	150	150	150	150	150	150	150	150	150	150	150	150	150	150	150
3D-SLS	150	150	150	150	150	150	150	150	150	150	150	150	150	150	150	150

Figure 6. The number of successfully tracked segments using two- or three-dimensional (2/3D) cardiovascular magnetic resonance based tissue tracking. Six lines with round points represent the number of tracked segments, and the chart below lists the detailed number. SRS, segmental radial peak strain; SCS, segmental circumferential peak strain; SLS, segmental longitudinal peak strain.

Table 4: The number of segments included for SRS assessment with 2/3D CMR-TT.

Segment	SRS			
	SAX-N_{2D} (%)	**LAX-N_{2D} (%)**	**Total-N_{2D} (%)**	**N_{3D} (%)**
1. Basal anterior	150 (100.0%)	146 (97.3%)	150 (100.0%)	150 (100.0%)
2. Basal anteroseptal	149 (99.3%)	144 (96.0%)	150 (100.0%)	150 (100.0%)
3. Basal inferoseptal	145 (96.7%)	143 (95.3%)	150 (100.0%)	150 (100.0%)
4. Basal inferior	109 (72.7%)	139 (92.7%)	147 (98.0%)	150 (100.0%)
5. Basal inferolateral	133 (88.7%)	140 (93.3%)	150 (100.0%)	150 (100.0%)
6. Basal anterolateral	150 (100.0%)	146 (97.3%)	150 (100.0%)	150 (100.0%)
7. Mid anterior	150 (100.0%)	143 (95.3%)	150 (100.0%)	150 (100.0%)
8. Mid anteroseptal	150 (100.0%)	143 (95.3%)	150 (100.0%)	150 (100.0%)
9. Mid inferoseptal	150 (100.0%)	144 (96.0%)	150 (100.0%)	150 (100.0%)
10. Mid inferior	150 (100.0%)	138 (92.0%)	150 (100.0%)	150 (100.0%)
11. Mid inferolateral	150 (100.0%)	141 (94.0%)	150 (100.0%)	150 (100.0%)
12. Mid anterolateral	150 (100.0%)	146 (97.3%)	150 (100.0%)	150 (100.0%)
13. Apical anterior	150 (100.0%)	150 (100.0%)	150 (100.0%)	150 (100.0%)
14. Apical septal	150 (100.0%)	150 (100.0%)	150 (100.0%)	150 (100.0%)
15. Apical inferior	150 (100.0%)	150 (100.0%)	150 (100.0%)	150 (100.0%)
16. Apical lateral	150 (100.0%)	150 (100.0%)	150 (100.0%)	150 (100.0%)

N (%) means the number (fraction) of segments with available segmental radial peak strain (SRS).

Abbreviations: 2/3D CMR-TT, two- or three-dimensional cardiovascular magnetic resonance based tissue tracking; SAX, short-axis; LAX, long-axis. (Qu et al., 2021) CC BY-NC-ND 4.0, https://creativecommons.org/licenses/by-nc-nd/4.0/

Table 5: The number of segments included for SCS and SLS assessment with 2/3D CMR-TT.

Segment	SCS		SLS	
	SAX-N_{2D} (%)	N_{3D} (%)	LAX-N_{2D} (%)	N_{3D} (%)
1. Basal anterior	150 (100.0%)	150 (100.0%)	146 (97.3%)	150 (100.0%)
2. Basal anteroseptal	149 (99.3%)	150 (100.0%)	144 (96.0%)	150 (100.0%)
3. Basal inferoseptal	145 (96.7%)	150 (100.0%)	143 (95.3%)	150 (100.0%)
4. Basal inferior	109 (72.7%)	150 (100.0%)	139 (92.7%)	150 (100.0%)
5. Basal inferolateral	133 (88.7%)	150 (100.0%)	140 (93.3%)	150 (100.0%)
6. Basal anterolateral	150 (100.0%)	150 (100.0%)	146 (97.3%)	150 (100.0%)
7. Mid anterior	150 (100.0%)	150 (100.0%)	143 (95.3%)	150 (100.0%)
8. Mid anteroseptal	150 (100.0%)	150 (100.0%)	143 (95.3%)	150 (100.0%)
9. Mid inferoseptal	150 (100.0%)	150 (100.0%)	144 (96.0%)	150 (100.0%)
10. Mid inferior	150 (100.0%)	150 (100.0%)	138 (92.0%)	150 (100.0%)
11. Mid inferolateral	150 (100.0%)	150 (100.0%)	141 (94.0%)	150 (100.0%)
12. Mid anterolateral	150 (100.0%)	150 (100.0%)	146 (97.3%)	150 (100.0%)
13. Apical anterior	150 (100.0%)	150 (100.0%)	150 (100.0%)	150 (100.0%)
14. Apical septal	150 (100.0%)	150 (100.0%)	150 (100.0%)	150 (100.0%)
15. Apical inferior	150 (100.0%)	150 (100.0%)	150 (100.0%)	150 (100.0%)
16. Apical lateral	150 (100.0%)	150 (100.0%)	150 (100.0%)	150 (100.0%)

N (%) means the number (fraction) of segments with available segmental circumferential peak strain (SCS) and segmental longitudinal peak strain (SLS). (Qu et al., 2021) CC BY-NC-ND 4.0, https://creativecommons.org/licenses/by-nc-nd/4.0/

3.2.1.2 Reference values of LV segmental strains

The reference values of LV segmental strains derived from 2D and 3D CMR-TT are presented in Table 6-8 and Figure 7. Compared with 2D SRS, 3D SRS was found to be significantly larger at basal and apical segments, and smaller at middle segments (P<0.05). 2D SCS and SLS show larger negative values than 3D SCS and SLS at most segments.

Table 6: Reference values of SRS measured with 2D and 3D CMR-TT.

Segment	SRS (%)		
	2D CMR-TT	**3D CMR-TT**	***P*-value**
1. Basal anterior	49.8 ± 17.9	59.3 ± 24.7	**0.001***
2. Basal anteroseptal	25.5 ± 11.4	31.8 ± 15.1	**<0.001***
3. Basal inferoseptal	19.1 ± 11.8	27.7 ± 14.1	**<0.001***
4. Basal inferior	35.6 ± 20.0	51.1 ± 22.8	**<0.001***
5. Basal inferolateral	66.7 ± 25.4	76.4 ± 31.3	**<0.001***
6. Basal anterolateral	75.7 ± 26.0	78.4 ± 31.6	0.249
7. Mid anterior	50.4 ± 15.2	39.8 ± 13.7	**<0.001***
8. Mid anteroseptal	36.0 ± 10.8	29.9 ± 12.6	**<0.001***
9. Mid inferoseptal	33.6 ± 9.7	26.1 ± 10.3	**<0.001***
10. Mid inferior	40.0 ± 14.7	31.9 ± 14.0	**<0.001***
11. Mid inferolateral	52.6 ± 16.8	37.8 ± 18.4	**<0.001***
12. Mid anterolateral	59.5 ± 19.5	43.6 ± 18.3	**<0.001***
13. Apical anterior	54.9 ± 19.7	68.2 ± 30.3	**<0.001***
14. Apical septal	48.2 ± 15.5	56.5 ± 23.5	**<0.001***
15. Apical inferior	51.2 ± 18.4	58.2 ± 24.3	**<0.001***
16. Apical lateral	50.3 ± 16.9	52.0 ± 22.8	0.264

Results are reported as mean ± standard deviation. *P<0.05. Abbreviations: SRS, segmental radial peak strain; 2/3D CMR-TT, two- and three-dimensional cardiovascular magnetic resonance based tissue tracking. (Qu et al., 2021) CC BY-NC-ND 4.0, https://creativecommons.org/licenses/by-nc-nd/4.0/

Table 7: Reference values of SCS measured with 2D and 3D CMR-TT.

Segment	SCS (%)		
	2D CMR-TT	**3D CMR-TT**	***P*-value**
1. Basal anterior	-26.5 ± 6.3	-19.8 ± 2.9	**<0.001***
2. Basal anteroseptal	-17.8 ± 6.5	-13.5 ± 3.5	**<0.001***
3. Basal inferoseptal	-12.1 ± 6.9	-14.2 ± 2.9	**<0.001***
4. Basal inferior	-18.0 ± 8.6	-14.5 ± 3.1	**<0.001***
5. Basal inferolateral	-27.8 ± 7.4	-14.9 ± 3.6	**<0.001***
6. Basal anterolateral	-29.5 ± 6.1	-18.5 ± 3.3	**<0.001***
7. Mid anterior	-21.0 ± 4.8	-20.5 ± 3.5	**0.029***
8. Mid anteroseptal	-19.9 ± 4.5	-15.5 ± 3.4	**<0.001***
9. Mid inferoseptal	-17.5 ± 4.5	-18.6 ± 3.9	**<0.001***
10. Mid inferior	-18.1 ± 5.7	-20.8 ± 3.5	**<0.001***
11. Mid inferolateral	-24.4 ± 6.0	-20.9 ± 4.0	**<0.001***
12. Mid anterolateral	-24.2 ± 5.6	-20.4 ± 4.1	**<0.001***
13. Apical anterior	-26.6 ± 4.4	-14.8 ± 3.2	**<0.001***
14. Apical septal	-24.6 ± 5.2	-13.7 ± 3.4	**<0.001***
15. Apical inferior	-25.8 ± 4.6	-19.3 ± 3.9	**<0.001***
16. Apical lateral	-26.8 ± 4.8	-18.8 ± 4.0	**<0.001***

Results are reported as mean ± standard deviation. *P<0.05. (Qu et al., 2021) CC BY-NC-ND 4.0, https://creativecommons.org/licenses/by-nc-nd/4.0/

Table 8: Reference values of SLS measured with 2D and 3D CMR-TT.

Segment	SLS (%)		
	2D CMR-TT	**3D CMR-TT**	***P*-value**
1. Basal anterior	-17.8 ± 6.0	-13.4 ± 4.5	**<0.001***
2. Basal anteroseptal	-11.7 ± 5.1	-12.4 ± 3.7	0.241
3. Basal inferoseptal	-12.6 ± 4.5	-10.5 ± 3.3	**<0.001***
4. Basal inferior	-18.1 ± 7.0	-9.3 ± 4.3	**<0.001***
5. Basal inferolateral	-24.7 ± 6.7	-12.4 ± 3.8	**<0.001***
6. Basal anterolateral	-26.3 ± 7.0	-12.6 ± 4.1	**<0.001***
7. Mid anterior	-26.2 ± 4.7	-20.7 ± 3.4	**<0.001***
8. Mid anteroseptal	-19.7 ± 3.9	-17.4 ± 3.4	**<0.001***
9. Mid inferoseptal	-20.6 ± 3.5	-17.1 ± 3.5	**<0.001***
10. Mid inferior	-22.9 ± 5.2	-19.3 ± 3.7	**<0.001***
11. Mid inferolateral	-23.2 ± 4.7	-21.0 ± 4.0	**<0.001***
12. Mid anterolateral	-26.6 ± 5.2	-20.4 ± 3.9	**<0.001***
13. Apical anterior	-21.5 ± 7.2	-15.0 ± 3.2	**<0.001***
14. Apical septal	-21.5 ± 4.0	-16.7 ± 3.8	**<0.001***
15. Apical inferior	-21.0 ± 6.3	-20.6 ± 4.6	0.464
16. Apical lateral	-18.6 ± 6.5	-18.9 ± 3.6	0.488

Results are reported as mean ± standard deviation. *P<0.05. (Qu et al., 2021) CC BY-NC-ND 4.0, https://creativecommons.org/licenses/by-nc-nd/4.0/

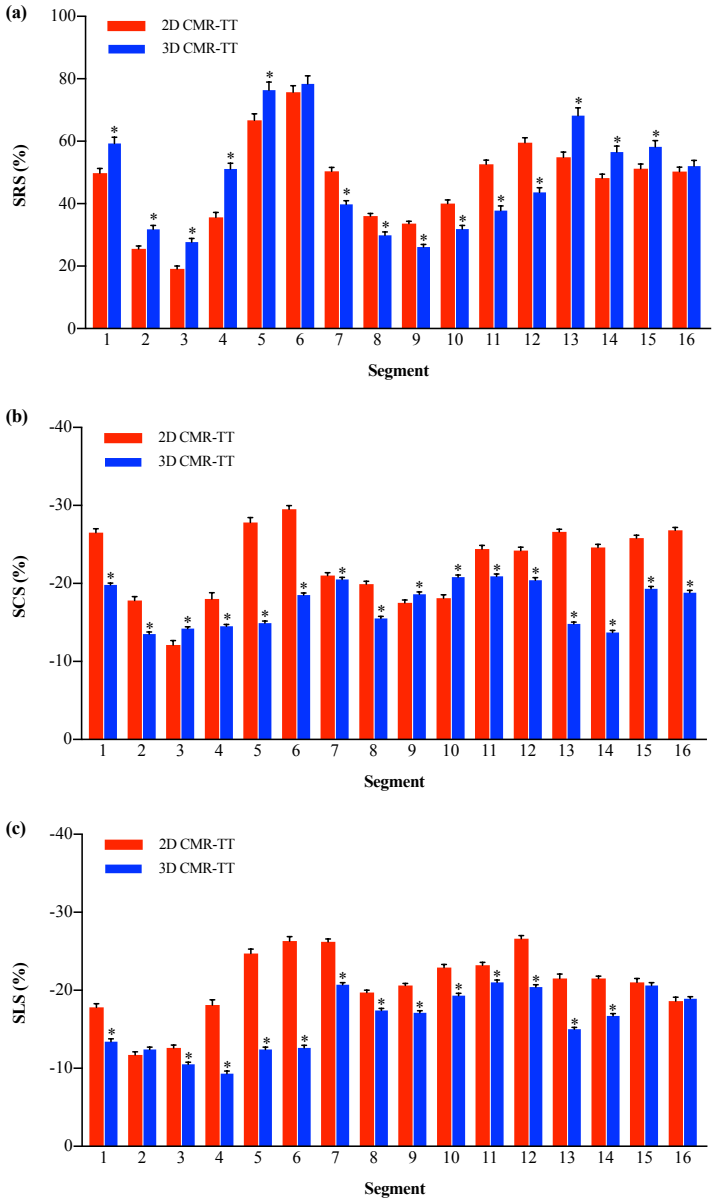


Figure 7. Comparison of left-ventricular (LV) segmental peak strains derived from two- and three-dimensional cardiovascular magnetic resonance based tissue tracking (2/3D CMR-TT). (a) SRS, segmental radial peak strain. (b) SCS, segmental circumferential peak strain. (c) SLS, segmental longitudinal peak strain. This figure provides intuitive expression of reference value and tendency of multi-dimensional strains at each segment in the context of 2D and 3D CMR-TT. Segment: 1.basal anterior, 2.basal anteroseptal, 3.basal inferoseptal, 4.basal inferior, 5.basal inferolateral, 6.basal anterolateral, 7.mid anterior, 8.mid anteroseptal, 9.mid inferoseptal, 10.mid inferior, 11.mid inferolateral, 12.mid anterolateral, 13.apical anterior, 14.apical septal, 15.apical inferior, 16. apical lateral. *P<0.05. (Qu et al., 2021) CC BY-NC-ND 4.0, https://creativecommons.org/licenses/by-nc-nd/4.0/

3.2.2 LV regional strains

The reference values of LV segmental strains derived from 2D and 3D CMR-TT are presented in Table 9-11.

The basal and apical RS measured by 3D CMR-TT were significantly larger than those measured by 2D CMR-TT as 54.1 ± 16.5% vs. 45.4 ± 10.0% and 58.7 ± 20.0% vs. 51.2 ± 14.7%. Whereas mid-cavity RS derived from 3D CMR-TT was significantly lower than that from 2D CMR-TT as 34.9 ± 10.5% vs. 45.4 ± 9.5% (P<0.001). 3D RCS and RLS were significantly lower than 2D RCS and RLS at all basal, mid-cavity and apical parts (P<0.001). In the context of 2D CMR-TT, the regional values ranked as base≈middle cavity<apex for RRS, middle cavity<base<apex for RCS and base<apex<middle cavity for RLS. While, in the context of 3D CMR-TT, it turned into the situation where middle cavity<base<apex for RRS, base<apex<middle cavity for RCS and base<apex<middle cavity for RLS (P<0.05).

Table 9: Reference values of basal, mid-cavity and apical RS measured with 2D and 3D CMR-TT.

Region	**RRS (%)**		
	2D CMR-TT	**3D CMR-TT**	***P*-value**
Basal	45.4 ± 10.0[a]	54.1 ± 16.5[ac]	**<0.001***
Mid-cavity	45.4 ± 9.5[a]	34.9 ± 10.5[ab]	**<0.001***
Apical	51.2 ± 14.7[bc]	58.7 ± 20.0[bc]	**<0.001***

Results are reported as mean ± standard deviation. **P*<0.05: 2D RRS vs. 3D RRS. [a]*P*<0.05: vs. apical RRS; [b]*P*<0.05: vs. basal RRS; [c]*P*<0.05: vs. mid-cavity SRS. Abbreviations: RS, radial peak strain; RRS, regional radial peak strain; 2/3D CMR-TT, two- or three-dimensional cardiovascular magnetic resonance based tissue tracking.

Table 10: Reference values of basal, mid-cavity and apical CS measured with 2D and 3D CMR-TT.

Region	RCS (%)		
	2D CMR-TT	**3D CMR-TT**	***P*-value**
Basal	-21.6 ± 2.7[ac]	-15.9 ± 2.5[ac]	**<0.001***
Mid-cavity	-20.8 ± 3.3[ab]	-19.4 ± 3.1[ab]	**<0.001***
Apical	-25.9 ± 3.6[bc]	-16.7 ± 2.8[bc]	**<0.001***

Results are reported as mean ± standard deviation. **P*<0.05: 2D RCS vs. 3D RCS. [a]*P*<0.05: vs. apical RCS; [b]*P*<0.05: vs. basal RCS; [c]*P*<0.05: vs. mid-cavity RCS. Abbreviations: CS, circumferential peak strain; RCS, regional circumferential peak strain; 2/3D CMR-TT, two- or three-dimensional cardiovascular magnetic resonance based tissue tracking.

Table 11: Reference values of basal, mid-cavity and apical LS measured with 2D and 3D CMR-TT.

Region	RLS (%)		
	2D CMR-TT	**3D CMR-TT**	***P*-value**
Basal	-18.4 ± 3.0[ac]	-11.8 ± 2.6[ac]	**<0.001***
Mid-cavity	-23.2 ± 2.2[ab]	-19.3 ± 3.0[ab]	**<0.001***
Apical	-20.7 ± 4.5[bc]	-17.8 ± 3.1[bc]	**<0.001***

Results are reported as mean ± standard deviation. **P*<0.05: 2D RLS vs. 3D RLS. [a]*P*<0.05: vs. apical RLS; [b]*P*<0.05: vs. basal RLS; [c]*P*<0.05: vs. mid-cavity RLS. Abbreviations: LS, longitudinal peak strain; RLS, regional longitudinal peak strain; 2/3D CMR-TT, two- or three-dimensional cardiovascular magnetic resonance based tissue tracking.

3.2.3 LV global strains

3.2.3.1 Reference values of LV 2/3D global strains

The values of 2D and 3D global mean strains and global peak strains were presented in Table 12 and Figure 8.

The MRS weren't significantly different as 46.8 ± 9.5% for 2D and 48.0±13.5% for 3D value (*P*=0.644). 2D MCS and MLS were stronger than their 3D counterparts as -22.6±2.9% vs. -17.4±2.6% and -20.8±2.2% vs. -16.1±2.3%, respectively (*P*<0.001). 3D GRS was comparable with 2D GRS as 44.4±13.0% vs. 41.7±9.5% (*P*=0.094), and 3D GCS and GLS were significantly less negative than 2D GCS and GLS as -17.0±2.7% vs. -22.0±3.3% and -15.4±2.3% vs. -18.6±2.7%, respectively (*P*<0.001). The magnitudes of all global peak strains were significantly lower than the corresponding global mean values (*P*<0.001).

Table 12: Reference values of LV global strains measured with 2D and 3D CMR-TT.

	2D CMR-TT	3D CMR-TT	*P*-value
Global mean strains (%)			
Global radial mean strain (MRS)	46.8 ± 9.5	48.0 ± 13.5	0.644
Global circumferential mean strain (MCS)	-22.6 ± 2.9	-17.4 ± 2.6	**<0.001***
Global longitudinal mean strain (MLS)	-20.8 ± 2.2	-16.1 ± 2.3	**<0.001***
Global peak strains (%)			
Global radial peak strain (GRS)	41.7 ± 9.5$^{\#}$	44.4 ± 13.0$^{\#}$	0.094
Global circumferential peak strain (GCS)	-22.0 ± 3.3$^{\#}$	-17.0 ± 2.7$^{\#}$	**<0.001***
Global longitudinal peak strain (GLS)	-18.6 ± 2.7$^{\#}$	-15.4 ± 2.3$^{\#}$	**<0.001***

Results are reported as mean ± standard deviation. *P<0.05: 2D strains vs. 3D strains. $^{\#}P$<0.05: global peak strains vs. global mean strains. Abbreviations: LV, left-ventricular; 2/3D CMR-TT, two- or three-dimensional cardiovascular magnetic resonance based tissue tracking. (Qu et al., 2021) CC BY-NC-ND 4.0, https://creativecommons.org/licenses/by-nc-nd/4.0/

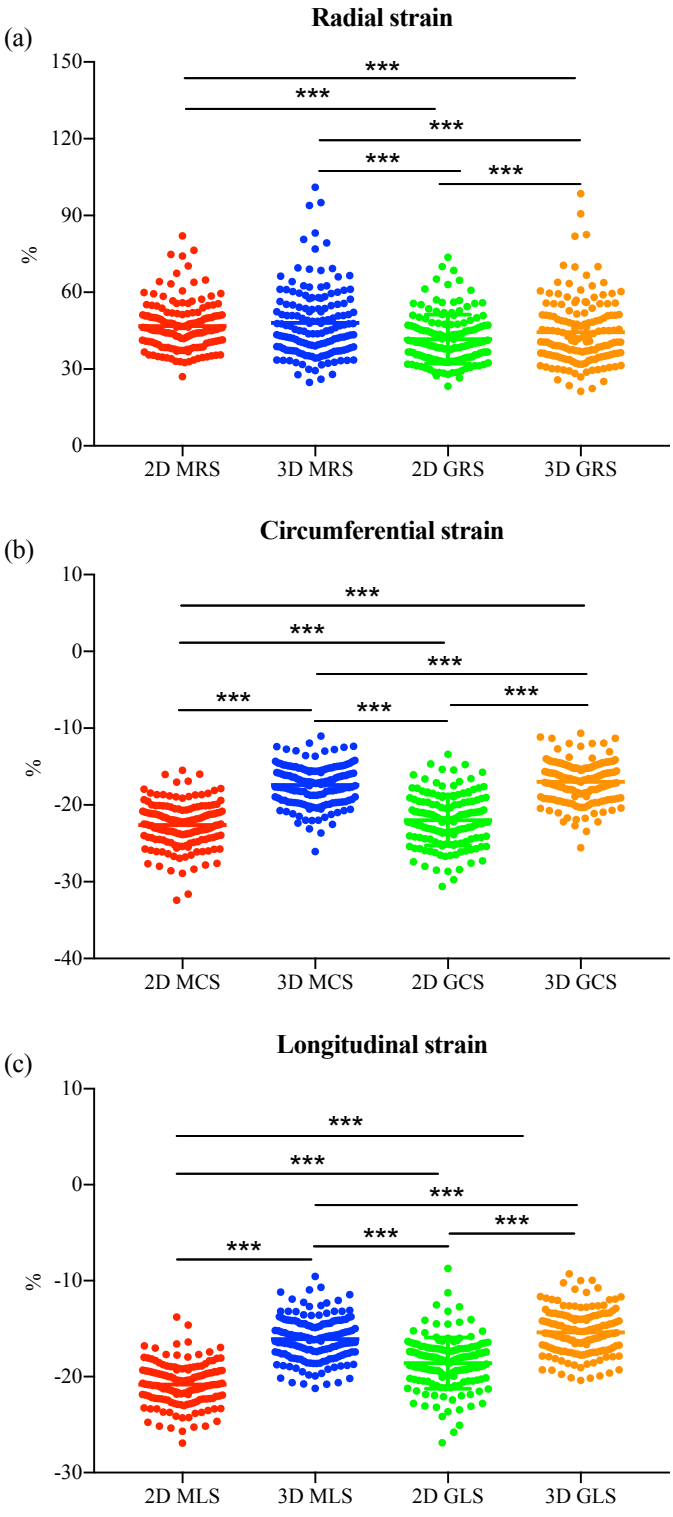


Figure 8. Comparisons among left-ventricular (LV) two- or three-dimensional (2/3D) global mean and peak strains. These scatter plots represent the data of LV radial, circumferential and longitudinal strains generated by two calculations in the context of both 2D and 3D cardiovascular magnetic resonance based tissue tracking. MRS, global radial mean strain; MCS, global circumferential mean strain; MLS, global longitudinal mean strain; GRS, global radial peak strain; GCS, global circumferential peak strain; GLS, global longitudinal peak strain. *P<0.05, ***P<0.001.

(Qu et al., 2021) CC BY-NC-ND 4.0, https://creativecommons.org/licenses/by-nc-nd/4.0/

As shown in Figure 9, 2D global mean strains were well correlated with 2D global peak strains with r resulted as 0.93-0.95. By comparison, 3D global mean strains were better correlated with 3D global peak strains with r resulted as 0.99. Meanwhile, 3D global peak strains were also highly correlated with 2D global peak strains with r resulted as 0.88 for radial, 0.89 for circumferential and 0.74 for longitudinal data.

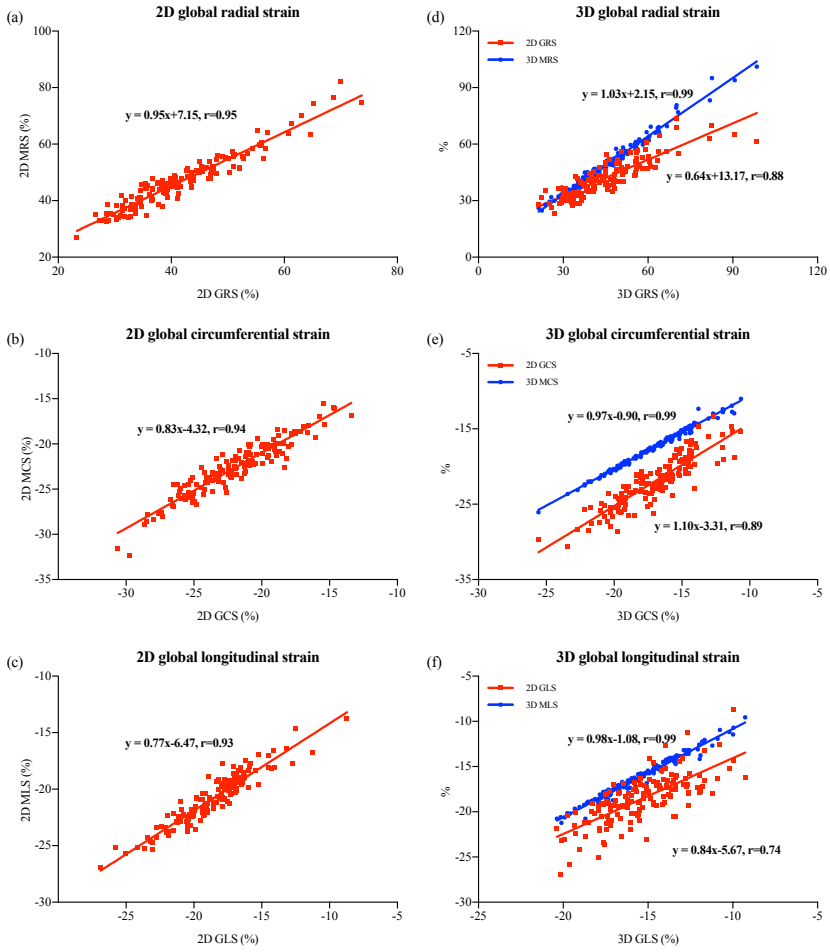


Figure 9. Correlations among left-ventricular (LV) two- or three-dimensional (2/3D) global mean or peak strains. (a-c) Correlation between LV 2D global radial, circumferential and longitudinal peak and mean strain (GRS, GCS, GLS and MRS, MCS, MLS). (d-f) Correlation between LV 3D global mean and peak strains, as well as the correlation between 2D and 3D global peak strains. Equations of linear regression and value of correlation coefficient (r) are added beside the corresponding lines (P<0.05). (Qu et al., 2021) CC BY-NC-ND 4.0, https://creativecommons.org/licenses/by-nc-nd/4.0/

3.2.3.2 Gender- and age-related difference of 3D global peak strains

Table 13 and Figure 10 illustrate the gender- and age-related difference and reference values of LV 3D global peak strains. In general, females showed larger absolute values of LV global peak strains than males as 47.1 ± 13.4% vs. 41.7 ± 12.0% for GRS, -17.5 ± 2.8% vs. -16.5 ± 2.5% for GCS and -16.0 ± 2.3% vs. -14.8 ± 2.2% for GLS (all P<0.05). The gender-related difference got more prominent with aging and turned to be significant in G_{61-80} subgroup. Additionally, the magnitude of 3D global peak strains of G_{61-80} subgroup were larger than G_{20-40} and G_{41-60} subgroups, implying the existence of age-related difference (P<0.05).

Table 13: Gender- and age-related differences of LV 3D global peak strains.

	G_{20-40}		G_{41-60}		G_{61-80}		Male	Female
	Male	Female	Male	Female	Male	Female	(n=75)	(n=75)
3D GRS (%)	41.2±14.7	41.9±9.5	40.4±11.1	47.0±16.6	43.6±10.1	52.4±11.4[a]	41.7±12.0	47.1±13.4[a]
3D GCS (%)	-16.4±2.4	-16.6±2.3	-15.8±2.4	-17.1±3.4	-17.2±2.5	-18.8±2.2[a]	-16.5±2.5	-17.5±2.8[a]
3D GLS (%)	-14.9±1.8	-15.7±2.3	-14.3±2.4	-15.2±2.6	-15.1±2.4	-17.0±1.8[a]	-14.8±2.2	-16.0±2.3[a]
3D GRS (%)	41.6±12.2		43.7±14.3		48.0±11.5[b]		-	-
3D GCS (%)	-16.5±2.3		-16.5±3.0		-18.0±2.5[bc]		-	-
3D GLS (%)	-15.3±2.1		-14.7±2.5		-16.1±2.3[c]		-	-

Results are reported as mean ± standard deviation. [a]P<0.05: male vs. female. [b]P<0.05: G_{20-40} vs. G_{61-80}; [c]P<0.05: G_{41-60} vs. G_{61-80}. Abbreviations: LV, left-ventricular; 3D, three-dimensional; GRS, global radial peak strain; GCS, global circumferential peak strain; GLS, global longitudinal peak strain. (Qu et al., 2021) CC BY-NC-ND 4.0, https://creativecommons.org/licenses/by-nc-nd/4.0/

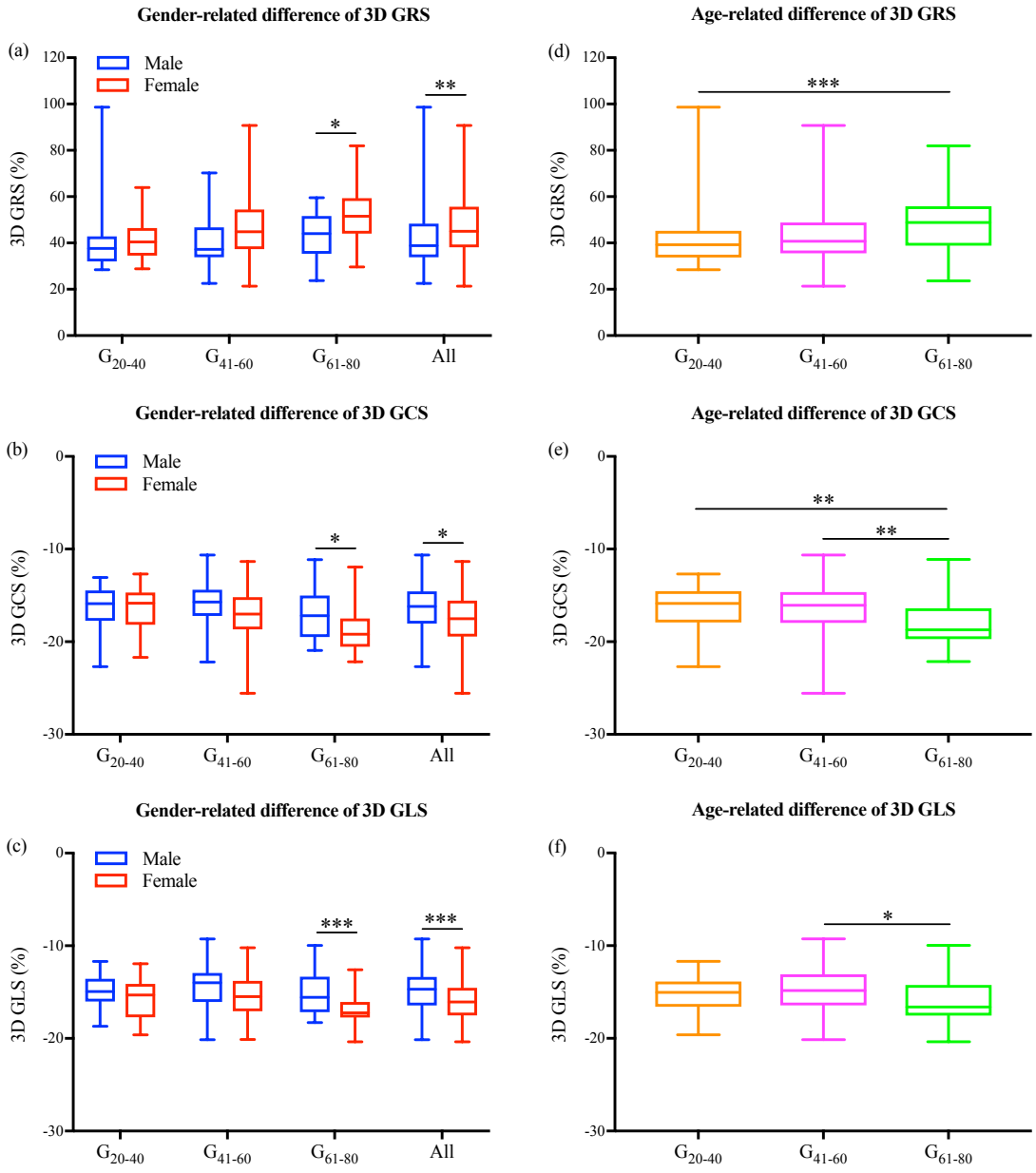


Figure 10. Gender- and age-related difference of left-ventricular three-dimensional (3D) global peak strains. (a-c). Gender-related difference of global radial, circumferential and longitudinal peak strain (GRS, GCS and GLS). (d-f). Age-related difference of GRS, GCS and GLS. The box-and-whisker plots represent the values between lower and upper quartile, and the middle line expresses the median in individual group. The minimum and maximum are shown at the end of whisker. $^{*}P<0.05$, $^{**}P<0.01$, $^{***}P<0.001$. (Qu et al., 2021) CC BY-NC-ND 4.0, https://creativecommons.org/licenses/by-nc-nd/4.0/

3.2.3.3 Correlation analysis of 3D global peak strains

Correlation analysis in Table 14 was applied to investigate the correlation between participants' characteristics and 3D global multi-dimensional peak strains. 3D global peak strains were weakly correlated with age and HR in radial, circumferential and longitudinal directions, respectively. BMI was found to be uncorrelated with neither GRS nor GLS (both $P>0.05$). The respective r between LVEDVI, LVESVI, LVEF and 3D global peak values were -0.56, -0.77, 0.73 for radial, 0.53, 0.71, -0.69 for circumferential and 0.48, 0.64, -0.61 for longitudinal strain. That meant the magnitude of 3D global peak strains showed positive correlation with LVEF at a good to excellent level, and negative correlation with LVEDVI and LVESVI ($P<0.05$).

Table 14: Correlation analysis of strains.

	GRS (%)		GCS (%)		GLS (%)	
	r	*P*	r	*P*	r	*P*
Age (year)	0.25	0.002*	-0.26	0.002*	-0.16	0.053
Height (cm)	-0.27	0.001*	0.23	0.004*	0.28	0.001*
Weight (kg)	-0.25	0.003*	0.30	<0.001*	0.20	0.013*
BSA (m^2)	-0.27	0.001*	0.31	<0.001*	0.25	0.002*
BMI (kg/m^2)	-0.10	0.217	0.19	0.022*	0.04	0.632
HR (bpm)	0.33	<0.001*	-0.31	<0.001*	-0.25	0.002*
LVMMI (g/m^2)	-0.44	<0.001*	0.39	<0.001*	0.37	<0.001*
LVEDVI (mL/m^2)	**-0.56**	<0.001*	**0.53**	<0.001*	**0.48**	<0.001*
LVESVI (mL/m^2)	**-0.77**	<0.001*	**0.71**	<0.001*	**0.64**	<0.001*
LVSVI (mL/m^2)	-0.21	0.011*	0.21	0.011*	0.19	0.022*
CI ($L/min/m^2$)	0.13	0.107	-0.11	0.172	-0.12	0.132
LVEF (%)	**0.73**	<0.001*	**-0.69**	<0.001*	**-0.61**	<0.001*

Abbreviation: GRS, global radial peak strain; GCS, global circumferential peak strain; GLS, global longitudinal peak strain; BSA, body surface area; BMI, body mass index; HR, heart rate; LVMMI, left-ventricular myocardial mass index; LVEDVI, left-ventricular end-diastolic volume index; LVESVI, left-ventricular end-systolic volume index; LVSVI, left-ventricular stroke volume index; CI, cardiac index; LVEF, left-ventricular ejection fraction; r, Pearson or Spearman correlation coefficient.

3.2.4 Reproducibility of LV 2/3D CMR-TT

Reproducibility of 2/3D CMR-TT was tested and the result was given in Table 15 and 16. At the segmental level, ICC of SRS, SCS and SLS were 0.83-0.99, 0.80-0.98 and 0.72-0.99 in the context of 2D CMR-TT, and 0.87-0.97, 0.86-0.98 and 0.84-0.99 in the setting of 3D CMR-TT. 3D CMR-TT presented higher CoV for SRS (18.59 ± 5.95% vs. 10.68 ± 3.46%, $P<0.001$), comparable CoV for SCS (9.79 ± 4.59% vs. 9.38 ± 4.53%, $P=0.80$), and SLS (6.88 ± 3.47% vs. 10.26 ± 6.65%, $P=0.10$) compared with 2D CMR-TT. At the global level, 2D and 3D global mean and peak strains showed high reproducibility (ICC≥0.97) and low variability (CoV≤5.96%) except 3D global radial mean strain (ICC=0.76, CoV=21.25%). It's interesting that the CoV reached the lowest as 0.57% when we measured LV GLS with 2D CMR-TT modality.

Table 15: Intra-observer reproducibility of 2D CMR-TT.

	2D SRS			2D SCS			2D SLS		
Seg.	MD ± SD (%)	ICC (95%CI)	CoV (%)	MD ± SD (%)	ICC (95%CI)	CoV (%)	MD ± SD (%)	ICC (95%CI)	CoV (%)
1	7.91±6.26	0.95(0.87-0.98)	12.66	2.20±1.89	0.94(0.85-0.98)	7.01	3.54±3.36	0.85(0.60-0.94)	20.07
2	3.73±4.93	0.92(0.79-0.97)	20.09	2.93±4.07	0.85(0.61-0.94)	24.13	1.04±0.93	0.98(0.96-0.99)	7.87
3	3.06±2.35	0.99(0.98-1.00)	11.30	2.48±2.20	0.94(0.84-0.98)	19.58	0.70±0.68	0.99(0.98-1.00)	5.11
4	7.61±5.41	0.95(0.88-0.98)	14.66	4.50±4.31	0.92(0.74-0.98)	23.34	2.64±2.75	0.95(0.87-0.98)	15.55
5	7.11±8.49	0.96(0.89-0.98)	12.28	2.86±3.47	0.89(0.69-0.96)	12.29	1.92±2.64	0.88(0.66-0.96)	9.93
6	9.52±6.90	0.96(0.90-0.98)	8.28	1.87±1.75	0.93(0.82-0.97)	5.86	1.42±2.20	0.97(0.92-0.99)	7.64
7	4.94±5.52	0.83(0.57-0.93)	11.32	1.08±1.24	0.93(0.83-0.97)	5.73	2.69±3.42	0.72(0.28-0.89)	13.37
8	3.19±3.00	0.98(0.94-0.99)	7.98	1.56±1.01	0.97(0.93-0.99)	4.77	1.23±1.33	0.96(0.89-0.98)	6.82
9	3.07±2.52	0.98(0.95-0.99)	7.31	2.08±1.49	0.95(0.87-0.98)	8.67	0.78±0.90	0.97(0.91-0.99)	4.35
10	5.09±3.84	0.94(0.85-0.98)	10.16	2.54±2.48	0.80(0.48-0.92)	13.84	2.22±2.53	0.94(0.85-0.98)	11.47
11	4.24±4.81	0.95(0.88-0.98)	10.02	1.91±1.97	0.95(0.87-0.98)	8.88	1.95±1.99	0.89(0.68-0.96)	8.37
12	5.06±4.01	0.97(0.92-0.99)	7.33	1.84±2.22	0.94(0.84-0.98)	10.07	1.09±1.21	0.98(0.94-0.99)	4.65
13	5.16±4.93	0.92(0.80-0.97)	10.06	1.37±1.42	0.83(0.58-0.93)	5.32	2.43±2.82	0.93(0.82-0.97)	14.72
14	3.47±3.41	0.97(0.91-0.99)	7.87	1.36±1.24	0.97(0.92-0.99)	5.29	1.21±1.09	0.94(0.86-0.98)	5.36
15	4.63±5.79	0.97(0.92-0.99)	13.01	1.22±1.11	0.98(0.94-0.99)	4.62	1.54±1.13	0.98(0.96-0.99)	6.05
16	3.25±2.88	0.96(0.89-0.98)	6.50	1.16±1.23	0.84(0.85-0.98)	4.77	1.80±1.50	0.97(0.92-0.99)	8.78
Mean	1.65±1.35	0.99(0.96-1.00)	2.98	0.76±0.61	0.97(0.92-0.99)	2.72	0.49±0.55	0.97(0.92-0.99)	2.68
peak	0.55±0.69	1.00(0.99-1.00)	1.72	0.29±0.51	0.99(0.98-1.00)	2.37	0.12±0.10	1.00(0.997-1.00)	0.57

Results are reported as mean difference (MD) ± standard deviation (SD). Abbreviations: 2D, two-dimensional; CMR-TT, cardiovascular magnetic resonance based tissue tracking; Seg., segment; SRS, segmental radial peak strain; SCS, segmental circumferential peak strain; SLS, segmental longitudinal peak strain; ICC, intra-observer correlation coefficient; CI, confidence interval; CoV, coefficient of variation. (Qu et al., 2021) CC BY-NC-ND 4.0, https://creativecommons.org/licenses/by-nc-nd/4.0/

Table 16: Intra-observer reproducibility of 3D CMR-TT.

	3D SRS			3D SCS			3D SLS		
Seg.	MD ± SD (%)	ICC (95%CI)	CoV (%)	MD ± SD (%)	ICC (95%CI)	CoV (%)	MD ± SD (%)	ICC (95%CI)	CoV (%)
1	10.80 ±10.50	0.87(0.66-0.95)	19.40	1.12±1.56	0.86(0.64-0.94)	7.93	1.31±0.98	0.98(0.94-0.99)	6.20
2	7.39±8.02	0.95(0.87-0.98)	22.12	1.01±0.82	0.96(0.90-0.98)	6.80	1.34±1.16	0.96(0.89-0.98)	9.47
3	6.90±8.25	0.97(0.93-0.99)	26.10	0.89±0.84	0.97(0.91-0.99)	6.27	1.50±1.02	0.93(0.83-0.97)	9.78
4	8.26±9.41	0.96(0.89-0.98)	19.54	0.92±0.86	0.97(0.94-0.99)	6.37	1.71±1.42	0.96(0.90-0.99)	17.07
5	16.20±17.19	0.93(0.81-0.97)	23.27	1.77±1.21	0.94(0.86-0.98)	8.86	1.96±1.77	0.92(0.79-0.97)	14.07
6	10.87±14.01	0.94(0.86-0.98)	18.07	1.42±1.32	0.96(0.89-0.98)	7.68	1.50±1.39	0.93(0.82-0.97)	10.19
7	3.87±2.13	0.96(0.89-0.98)	6.09	0.60±0.78	0.97(0.92-0.99)	4.01	1.40±1.41	0.89(0.73-0.96)	7.46
8	4.80±5.02	0.87(0.67-0.95)	19.04	1.04±0.89	0.98(0.94-0.99)	5.66	1.41±1.12	0.94(0.85-0.98)	7.00
9	3.98±4.90	0.93(0.81-0.97)	19.95	1.07±0.95	0.98(0.95-0.99)	5.12	0.90±0.71	0.99(0.97-1.00)	4.19
10	4.69±6.60	0.90(0.74-0.96)	24.09	1.49±1.13	0.96(0.90-0.98)	5.76	1.12±1.09	0.97(0.92-0.99)	5.90
11	4.97±4.28	0.94(0.85-0.98)	14.57	1.23±0.86	0.97(0.91-0.99)	4.32	0.93±1.01	0.98(0.95-0.99)	5.15
12	6.60±7.61	0.94(0.84-0.98)	21.23	0.67±0.76	0.98(0.96-0.99)	3.84	1.39±1.05	0.95(0.88-0.98)	5.45
13	5.60±5.58	0.96(0.89-0.98)	10.27	0.68±0.55	0.98(0.96-0.99)	3.89	1.25±1.71	0.84(0.86-0.98)	13.75
14	4.61±3.63	0.97(0.94-0.99)	7.89	1.19±1.56	0.92(0.81-0.97)	11.86	1.79±1.78	0.93(0.83-0.97)	12.83
15	8.33±11.54	0.92(0.80-0.97)	24.64	1.67±2.88	0.90(0.75-0.96)	17.14	1.92±3.00	0.92(0.80-0.97)	20.00
16	6.65±9.39	0.95(0.86-0.98)	21.16	1.16±0.77	0.92(0.80-0.97)	4.52	1.33±1.30	0.90(0.75-0.96)	8.12
Mean	11.15±9.63	0.76(0.40-0.91)	21.25	0.41±0.35	0.99(0.98-1.00)	2.10	0.50±0.43	0.98(0.95-0.99)	2.88
Peak	2.68±2.38	0.98(0.94-0.99)	5.96	0.42±0.36	0.99(0.98-1.00)	2.26	0.57±0.45	0.98(0.94-0.99)	3.14

Results are reported as mean difference (MD) ± standard deviation (SD). (Qu et al., 2021) CC BY-NC-ND 4.0, https://creativecommons.org/licenses/by-nc-nd/4.0/

3.3 RVFW strain measurement

3.3.1 RVFW global, regional and segmental longitudinal peak strains

RVFW global, regional and segmental peak LS (GLS, RLS and SLS) derived from 2D CMR-TT are illustrated in Table 17. The GLS_{myo} was comparable with GLS_{endo} as -24.9 ± 5.2% vs. -24.9 ± 5.0% (P>0.05), and resulted significantly different from GLS_{epi} as -24.9 ± 5.2% vs. -25.1 ± 5.2% (P<0.05). GLS_{endo} and GLS_{epi} were both well correlated with GLS_{myo} (R^2=0.97, P<0.05. Figure 11).

We also found that there was a base-to-apex gradient of RLS. The basal and middle-cavity RLS were significantly larger than apical RLS (P<0.05), while basal and middle-cavity RLS were comparable with each other.

Table 17: Reference values of RVFW global, regional and segmental longitudinal peak strains.

	HV (n=150)		**HV (n=150)**		**HV (n=150)**
GLS (%)		**RLS_{myo}** (%)		**SLS_{myo}** (%)	
GLS_{myo}	-24.9±5.2	**Basal**	-27.1±7.2	**Segment 1**	-26.2±9.0
GLS_{endo}	-24.9±5.0	**Mid-cavity**	-27.2±4.9	**Segment 2**	-28.1±6.4
GLS_{epi}	-25.1±5.2	**Apical**	-19.8±6.6	**Segment 3**	-28.3±5.6
				Segment 4	-25.9±5.6
				Segment 5	-23.2±5.8
				Segment 6	-16.5±8.9

Results are reported as mean ± standard deviation. Abbreviations: HV, healthy volunteer; GLS, global longitudinal peak strain; RLS, regional longitudinal strain; SLS, segmental longitudinal peak strain; GLS_{myo}, global longitudinal peak strain of myocardium; GLS_{endo}, global longitudinal peak strain of endocardium; GLS_{epi}, global longitudinal peak strain of epicardium. Modified from (Qu et al., 2020) CC BY 4.0, http://creativecommons.org/licenses/by/4.0/

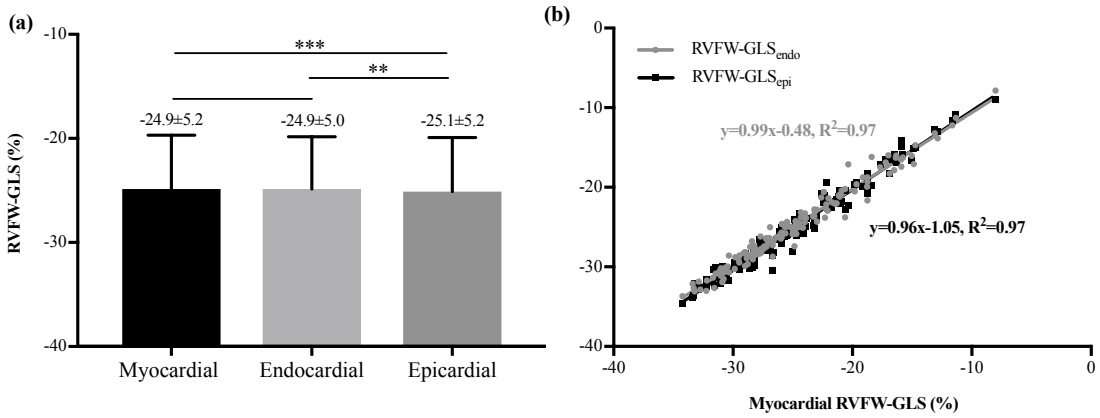


Figure 11. The reference values of three types of right-ventricular free wall global longitudinal peak strain (RVFW-GLS) and the correlation among them. (a) The normal values of RVFW-GLS of myocardium, endocardium and epicardium (RVFW-GLS_{myo}, RVFW-GLS_{endo}, RVFW-GLS_{epi}). GLS_{myo} was comparable with GLS_{endo} and significantly different from GLS_{epi}. (b) GLS_{endo} and GLS_{epi} were highly correlated with GLS_{myo} (R^2=0.97). $^{**}P$<0.01, $^{***}P$<0.001. (Qu et al., 2020) CC BY 4.0, http://creativecommons.org/licenses/by/4.0/

3.3.2 Gender- and age-related differences of RVFW-GLS

The gender- and age-specific reference values are shown in Table 18. Females showed larger magnitude of GLS_{myo}, GLS_{endo} and GLS_{epi} than males in $G_{41\text{-}60}$ and $G_{61\text{-}80}$ subgroups (P<0.05). While, there was no age-related difference of GLS_{myo} in both gender groups (P>0.05). The correlation analysis also proved that there was no correlation between age and GLS_{myo} (r=-0.031, P=0.703, Figure 12).

Table 18: Gender- and age-related differences of RVFW-GLS.

	G_{20-40}		G_{41-60}		G_{61-80}		Male	Female
	Male	**Female**	**Male**	**Female**	**Male**	**Female**	**(n=75)**	**(n=75)**
GLS_{myo} (%)	-24.8±5.2	-24.5±5.4	-23.3±4.7	-26.5±5.2*	-22.8±4.9	-27.2±4.7*	-23.7±4.9	-26.1±5.2*
GLS_{endo} (%)	-25.0±5.2	-24.2±5.2	-23.7±4.5	-26.4±5.0	-22.7±5.0	-27.1±4.4*	-23.8±4.9	-25.9±5.0*
GLS_{epi} (%)	-25.0±5.1	-24.7±5.8	-23.6±4.9	-26.6±5.1*	-23.4±5.0	-27.5±4.6*	-24.0±5.0	-26.2±5.2*

Results are reported as mean ± standard deviation. **P*<0.05: males vs. females. Abbreviations: RVFW-GLS, right-ventricular free wall global longitudinal peak strain; GLS_{myo}, global longitudinal peak strain of myocardium; GLS_{endo}, global longitudinal peak strain of endocardium; GLS_{epi}, global longitudinal peak strain of epicardium.

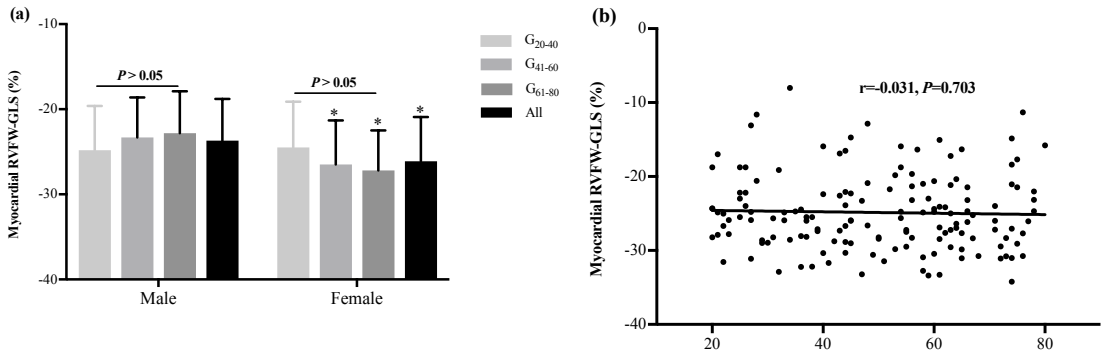


Figure 12. The reference values of right-ventricular free wall global longitudinal strain of myocardium (RVFW-GLS_{myo}) and its gender- and age-related differences. (a) Females presented with larger magnitude of GLS_{myo} than males in in G_{41-60} and G_{61-80} subgroups. No age-associated difference was detected in each gender group. *P<0.05: significant difference between males and females in the same age subgroup. (b) The correlation between age and RVFW-GLS_{myo}. There was no correlation between age and RVFW-GLS_{myo} since Spearman correlation coefficient (r) resulted as -0.031 (P=0.703). (Qu et al., 2020) CC BY 4.0, http://creativecommons.org/licenses/by/4.0/

3.3.3 Gender- and age-related differences of RVFW-RLS and SLS

The reference values of RLS and SLS are presented in Table 19. Among the whole population, the LS within middle-cavity and apical regions and segments presented gender-related differences in the absence of age-related dissimilarity. Females showed significantly larger magnitude of RLS than males in the middle-cavity and apical parts (P<0.05).

Table 19: Gender- and age-related differences of RVFW regional and segmental longitudinal peak strains.

	G_{20-40}		G_{41-60}		G_{61-80}		Male	Female
	Male	**Female**	**Male**	**Female**	**Male**	**Female**	**(n=75)**	**(n=75)**
RVFW-RLS (%)								
Basal	-28.1±7.4	-25.9±9.8	-27.9±5.9	-27.4±6.1	-24.6±6.6	-29.1±6.2*	-26.8±6.8	-27.5±7.6
Mid-cavity	-26.2±5.2	-26.0±5.7	-25.8±4.0	-28.9±4.0*	-26.5±5.1	-29.5±4.0*	-26.2±4.8	-28.1±4.8*
Apical	-18.1±5.4	-22.8±7.1*	-17.8±5.4	-21.8±8.5	-17.3±5.4	-21.2±5.8*	-17.8±5.4	-21.9±7.1*
RVFW-SLS (%)								
Segment 1	-27.2±8.7	-24.5±12.9	-27.2±7.6	-26.9±7.2	-23.0±7.7	-28.4±8.4*	-25.8±8.2	-26.6±9.8
Segment 2	-29.0±6.7	-27.3±8.5	-28.5±5.3	-27.8±6.1	-26.2±6.5	-29.7±4.7	-27.9±6.2	-28.3±6.6
Segment 3	-27.5±6.0	-27.0±6.4	-28.0±4.5	-29.2±5.6	-27.2±6.2	-30.7±4.5*	-27.6±5.5	-29.0±5.7*
Segment 4	-24.9±5.6	-25.1±6.8	-23.6±5.2	-28.5±4.2*	-25.1±6.0	-28.3±4.2	-24.5±5.5	-27.3±5.4*
Segment 5	-22.7±5.1	-24.7±6.0	-21.4±4.5	-25.2±6.7*	-20.3±5.7	-24.9±5.3*	-21.5±5.1	-24.9±5.9*
Segment 6	-13.6±7.3	-20.9±10.1*	-14.3±8.6	-18.4±11.3	-14.3±5.9	-17.5±7.7	-14.1±7.2	-18.9±9.8*

Results are reported as mean ± standard deviation. *P<0.05: males vs. females. Abbreviations: RVFW, right-ventricular free wall; RLS, regional longitudinal peak strain; SLS, segmental longitudinal peak strain. Modified from (Qu et al., 2020)

CC BY 4.0, http://creativecommons.org/licenses/by/4.0/

3.3.4 Correlation analysis of RVFW-GLS$_{myo}$

The correlation relationship between baseline, RV demographic, functional parameters and RVFW-GLS$_{myo}$ are presented in Table 20. As seen, weakly positive correlation between height, RVEDVI, RVESVI and RVFW-GLS$_{myo}$, as well as weakly negative correlation between HR, RVEF and RVFW-GLS$_{myo}$ were demonstrated (P<0.05).

Table 20: Correlation analysis of RVFW-GLS$_{myo}$.

	RVFW-GLS$_{myo}$ (%)			**RVFW-GLS$_{myo}$ (%)**	
	r	*P*		r	*P*
Age (year)	-0.031	0.703	RVEDVI (mL/m^2)	**0.285**	<0.001
Height (cm)	0.248	0.002	RVESVI (mL/m^2)	**0.330**	<0.001
Weight (kg)	0.092	0.262	RVSVI (mL/m^2)	0.101	0.221
BSA (m^2)	0.145	0.076	RVEF (%)	**-0.375**	<0.001
BMI (kg/m^2)	-0.030	0.716			
HR (bpm)	**-0.337**	<0.001			

Abbreviation: RVFW-GLS$_{myo}$, right-ventricular free wall global longitudinal peak strain of myocardium; BSA, body surface area; BMI, body mass index; HR, heart rate; RVEDVI, right-ventricular end-diastolic volume index; RVESVI, right-ventricular end-systolic volume index; RVSVI, right-ventricular stroke volume index; RVEF, right-ventricular ejection fraction; r, Pearson or Spearman correlation coefficient.

4 Discussion

This study comprehensively investigated the feasibility and reproducibility of 2/3D CMR-TT for quantifying biventricular global, regional and segmental multi-dimensional strains with CVI[42] software package. We also established gender- and age-related reference values and performed the correlation analysis of biventricular global strains among 150 healthy volunteers without cardiovascular diseases.

The major findings of this study are as follows: (i) CMR-TT could generate LV and RV global, regional and segmental strain values by tracking myocardial reference points throughout the whole cardiac cycle automatically; (ii) LV strain values measured with 2D and 3D CMR-TT were significantly different at global, regional and segmental levels; females and elderly subjects presented significantly larger magnitude of LV global systolic peak strains than males and young subjects; (iii) RVFW-LS of females was more negative than that of males, especially in the elderly group; and (iv) a base-to-apex gradient existed in biventricular strains, the LV longitudinal deformation in middle cavity was the most aggressive, while the RV longitudinal shortening in apex was weaker than that in base.

4.1 The measurement of LV and RV strains using CMR-TT technique

CMR has the advantages of high spatial and temporal resolution, good soft tissue contrast and high coverage without exposure to ionizing radiation and iodinated intravenous contrast medium, it has become the gold standard for evaluating function and deformation of heart. CMR-TT technique is emerging as an advanced technique contributing to quantifying myocardial mechanical deformation. Its principle is based on identifying and tracking

comparable tissue features between frames throughout the cardiac cycle (Pedrizzetti et al. 2016). The good agreement between CMR-TT and conventional CMR tagging has been validated (Cao et al. 2018). Meanwhile, the images used for CMR-TT are acquired with widely used SSFP sequence, which avoids additional scanning and then results in a more practical and time saving approach compared with tissue tagging (de Siqueira et al. 2016). Furthermore, CMR-TT presents to be advantageous for its sensibility and convenience to perform offline post-processing analysis (Scatteia et al. 2017). The studies about myocardial strain assessment using CMR-TT are still limited. Even though CMR-TT belongs to CMR-FT technique, reference values of strain weren't interchangeable between vendors and couldn't be simply used in other conditions (Barreiro-Perez et al. 2018; Schuster et al. 2015). Traditionally, EF calculated as the percentage of volumetric changes is regarded as a powerful and independent parameter to evaluate heart contractile function. However, it's not able to quantitatively assess myocardial global and regional deformation. By comparison, myocardial strain exerts a sensitive role to detect subclinical alterations of myocardial function and mechanical abnormalities against EF (Park JH et al. 2014).

The commercial software for strain analysis was initially developed for LV measurement. Nowadays, there is strong evidence showing that RV dysfunction plays a critical role in developing cardiovascular diseases (Haddad et al. 2008a; Sanz et al. 2019). The main function of RV is pumping the venous return into the pulmonary arteries and lungs. Impaired RV function is probably involved in cardiomyopathies, and congenital, ischemic, valvular and pulmonary heart diseases (Prasad and Lota 2017; Sabe et al. 2016; Voelkel et al. 2006).

Therefore, the evaluation of RV function has gained clinical relevance over recent years. The traditional index used in the clinical routine is RVEF and RVSV, it may not change at the early stage of diseases (de Siqueira et al. 2016). RV measurement of deformation is challenging due to its complex anatomical shape, thin trabeculated myocardium, significant load dependence and variability of filling with respiration (de Siqueira et al. 2016; Haddad et al. 2008b). CMR enables the collection of high spatial and temporal resolution data (Klinke et al. 2013) and overcomes the narrow or even non-existent acoustic windows of echocardiography caused by RV retrosternal position and thin myocardium (3-5mm) (Mouton et al. 2017; Suever et al. 2017). However, studies providing the reference values of RV myocardial strains are still limited.

The longitudinal shortening is the major motivation of RV contraction, and the normal RV function was revealed highly dependent on longitudinal shortening (Carlsson et al. 2007). Considering the interventricular septum is a constituent part of the LV and only contributes 20% to RV systolic performance (Sanz-de la Garza M et al. 2019), RVFW-LS is superior to describe RV function and deformation. In this study, we focused on RVFW global, regional and segmental LS derived from four-chamber LAX cine images of heart. The GLS here is literally “global”, because it neglects the involvement of septum to the contraction and function of RV. RVFW-GLS was reported to be the most accurate functional maker correlating with the degree of RV myocardial fibrosis in patients with advanced heart failure (Sanz-de la Garza M et al. 2019). It also works well as a remarkable prognostic marker in acute non-massive pulmonary embolism with AUC as 0.754 (Lee et al. 2019). In addition,

intraoperative RV functional decline was found to be primarily related with mutilations in RVFW deformation rather than that of the interventricular septum (Rong et al. 2019). It is also capable to provide important diagnostic values in patients with depressed RVEF (AUC=0.918) (Focardi et al. 2015), RV pressure overload (AUC=0.95) (Hardegree et al. 2013), proximal right coronary artery lesion-induced ischemic heart disease (AUC=0.79) (Chang et al. 2014).

The CVI[42] software package provides both of 2D and 3D modes for measuring LV myocardial deformation. Considering there is no consensus on the specific algorithm chosen for assessment and no standardized protocol for further clinical application, feasibility and reproducibility of CMR-TT at 2D and 3D level need to be investigated. Liu et al selectively measured LV 2D strains at SAX mid sections or horizontal LAX plane and then probed the reproducibility of 2D and 3D CMR-TT in measuring global peak strains among 100 subjects. Analysis of the reference values, feasibility and reproducibility of segmental strains was not performed (Liu et al. 2018c). In our study, we fully investigated LV 2D and 3D global, regional and segmental strain (including reference values and correlation analysis) in all directions among a larger sample-size healthy population (n=150).

4.2 Feasibility and reproducibility of 2/3D CMR-TT on LV strain measurement

When we analyzed LV SRS and SCS with SAX cine images, 2D CMR-TT presented obvious limitations in the quantitative measurement in the basal part, especially in the basal inferior and posterior segments. The fatal weakness put a constraint on the application of 2D CMR-TT in assessing segmental deformation, which was coincident with Maceira's report

(Maceira et al. 2018). The complex architecture of the mitral annuls is probably responsible for the poor tracking of the basal segments (Scatteia et al. 2017). By comparison, 3D CMR-TT could complete the measurement of 100% segments with the construction of LV 3D model. We also demonstrated that the greatest variability of normal values of SRS in this study is in coincidence with previous studies, which may be due to the most significant thickening gradient in the radial plane (Yingchoncharoen et al. 2013).

The magnitudes of strain values provided by 3D CMR-TT were significantly smaller than those by 2D CMR-TT in most segments. This may be associated with out-of-plan motion and algorithm-determined geometric assumption of 3D CMR-TT technique (Berganza et al. 2017; Mochizuki et al. 2013). In terms of the tracking reproducibility, 3D CMR-TT presented with higher intra-observer variability and worse reproducibility in radial, comparable intra-observer variability and reproducibility in circumferential and lower intra-observer variability and better reproducibility in longitudinal tracking than 2D CMR-TT at segmental level.

We found a base-to-apex gradient of LV regional systolic peak strains, which could be associated with the differences in wall thickness, myocardial architecture and local stress between and base and apex (Bogaert and Rademakers 2001; Mathur et al. 2019). Pathologies of the myocardium such as hypertrophy, fibrosis, inflammation may impair the physical base-to-apex gradient of LV contractility.

It is a consensus that global tracking is more reliable and preferred than local tracking since it estimates an average process where errors may partly cancel out (Schuster et al. 2015).

Four categories of parameter, 2D and 3D global mean and peak strains, could be used to describe LV deformation. 2D CMR-TT worked much better than 3D CMR-TT in computing MRS (CoV=5.96% vs. 21.25%). Considering that global mean strains needs additional averaging of all segmental strains, the time spent on sorting and calculating data may limit their application in busy clinical settings. 3D CMR-TT emerges later than 2D CMR-TT, it took the out-of-plane motion of myocardium into consideration. Meanwhile, 3D global peak strain could be derived by the software automatically after the tracking process, it would be a precise and efficient predictor to reflect LV global deformation. However, the reference values of global peak strains measured with 3D CMR-TT are still limited. In the healthy cohort of our study, LV 3D global peak values resulted as 44.4±13.0% for radial, -17.0±2.7% for circumferential and -15.4±2.3% for longitudinal strain.

4.3 Reference values of RV strains

CMR-TT can not only track myocardial pixels but also endocardial and epicardial contours. In this study, we only analyzed RVFW, namely RV lateral wall, hence the reference values generated couldn't be simply utilized to estimate the mechanical deformation of the whole RV myocardium. In fact, the RVFW is thinner and thus more potential to present higher longitudinal deformation against pulmonary resistance compared to the interventricular septum (Rimbas et al. 2016). The other possible clarification for less negative strain of septum is that the septum contracting to sustain both of RV loading conditions and LV afterload attenuates its contribution in RV movement (Meris et al. 2010).

We investigated the RVFW-GLS at all levels and the reference value of RVFW-GLS_{myo} resulted as -24.9±5.1%, which was close to the value -24.2±3.59% estimated by Liu et al among 100 normal healthy subjects (Liu et al. 2018b). We also discovered that RVFW-GLS_{myo} was highly correlated with RVFW-GLS_{endo}, and RVFW-GLS_{epi} values weren't substantially different with RVFW-GLS_{endo}. The LV-GLS of endocardium was reported to have the ability to uncover the impairment of LV at the early stage due to the structure of helical ventricular myocardial band (Sengupta et al. 2006), however, whether there is difference among these three types of RVFW-GLS in detecting RV dysfunction remains to be investigated in the future.

The base-to-apex gradient of RVFW-RLS was revealed and resulted as -27.1±7.2%, -27.2±4.9% and -19.8±6.6% from base to apex (P<0.05). RVFW-RLS in the basal and mid-cavity regions are comparable, and reached the lowest in the apical territories. Our conclusion is exactly comparable with the finding from a meta-analysis of 226 healthy children (<21 years of age) from 10 studies (Levy et al. 2014) and others' researches (Kemal et al. 2017; Rimbas et al. 2016). This physiological principle of base-to-apex heterogeneity may help differentiate the early alteration of RV myocardial contractility or afterload among patients with various pathological changes. Furthermore, even though the reproducibility of segmental strain is lower than global parameters (Mirea et al. 2019), the establishment of reference values of segmental strains and attention paid on the segmental alterations contribute to a better understanding and localization of impaired myocardium.

The reproducibility of measuring RVFW-LS with CMR-TT wasn't evaluated in our study. However, other researchers have scrutinized the feasibility and reproducibility of this technique and obtained satisfying results. According to the result from Liu et al, the ICC of RVFW-GLS was 0.92 (95% CI: 0.61–0.98) for intra-observer and 0.87 (95% CI: 0.57–0.97) for inter-observer variability (Liu et al. 2018a), which is comparable with the data from Truong (Truong et al. 2017).

4.4 Gender- and age-related difference of LV and RV global peak strains

Considering the difference of morphologic features between males and females and the young and the old, the establishment of specific reference values for the different groups is necessary.

Actually, gender-related difference of LV strain is still a matter of debate. Andre et al found females had more negative GCS and GLS compared with males, whereas males had higher GRS (Andre et al. 2015). However, Taylor et al found females had similar GRS and GCS along with more negative GLS compared with males (Taylor et al. 2015). In our study, healthy females showed significantly higher absolute values of global systolic peak strains than males, which were positively correlated with EF and inversely correlated with LVMMI, LVEDVI and LVESVI (Taylor et al. 2015). Interestingly, we observed that females merely presented significantly higher strains than males in G_{61-80} rather than G_{20-40} or G_{41-60}, implying the age-related heterogeneity with respect to gender-related difference. The augmented gender-related difference of strains in the elderly population may be caused by the more substantial deterioration of diastolic dysfunction in females. As reported, females

tend to develop diastolic dysfunction with a more normal EF, and myocardium turns to be stiff and inflexible with aging (Ferreira et al. 2015; Okura et al. 2009). The age-related difference of global peak strains along with LV volume and HR were detected between G_{20-40} and G_{61-80}. Therefore, we hypothesize that the higher magnitude of systolic strains of elderly population may be a mechanical compensation for slower HR and myocardial remodeling due to natural aging (Cheng et al. 2009; Hung et al. 2017).

Gender-related differences of RVFW-LS have been discussed before. Truong et al analyzed the RVFW-GLS among 50 patients (4-81 years old) without known cardiac pathology with the same software package. He demonstrated that the GLS was comparable between males and females as -22.22 ±3.4% and -22.80 ±3.5% (Truong et al. 2017). Liu et al also derived a similar conclusion as RVFW-GLS was -23.9 ±3.59% for males and -24.6 ±3.59% for females (P=0.34) (Liu et al. 2018a). However, our study reports a significant higher magnitude of RVFW-GLS_{myo} in females compared with that in males as -26.1±5.2% vs. -23.7±4.9% (P<0.05) on the basis of a larger sample size. Our finding is consistent with previous studies including the largest study performed among 276 healthy volunteer by Muraru et al (Muraru et al. 2016). We hypothesized that the gender-related difference of GLS was probably in the response of different RV size and systolic function, since males presented higher RVEDVI, RVESVI and lower RVEF.

With the potential age-related increase in pulmonary artery pressure, pulmonary vascular resistance, cardiomyocyte loss and subsequent replacement by fibrosis, RVFW mechanical function was supposed to decrease with aging (Chia et al. 2014). While, to our surprise, we

found neither age-related difference of RVFW-GLS_{myo} in both gender groups nor correlation between age and RVFW-GLS_{myo}. This finding is in line with the finding of a series of researches (Muraru et al. 2016; Salehi Ravesh et al. 2018; Truong et al. 2017). This discovery might simplify the establishment of reference values and clinical use of RVFW-GLS_{myo}. However, normative data from multicenter and larger size of population are still necessary for the further validation.

4.5 Limitations of this study

There were several limitations to this study. Firstly, it's a single-center study among 150 healthy volunteers, further investigations in multiple centers with larger sample size are still necessary to further clarify the intrinsic principle of biventricular strains. Secondly, the quality of semi-automated delineation of myocardial borders and automated tracking of tissue patterns may be more influenced by poor image quality and contour conspicuity. Therefore, we inspected and corrected the contours manually after the first tracking to check the tracking quality and made modifications if needed, this procedure might cause minor subjective bias. However, it's an inevitable problem of this kind of software. Thirdly, CMR-TT software package was primarily designed for LV assessment, it's challenging to quantify RV myocardial deformation due to the thin-thickness wall and crescent shape of RV. So in this study, we merely focused on the deformation in the longitudinal direction with four-chamber LAX cine images. Fourthly, we didn't compare CVI[42] software package with others like tissue tagging and FT. Nevertheless, previous studies have proved CMR-TT of good reproducibility compared with CMR tagging and feature tracking (Barreiro-Perez et al. 2018;

Schuster et al. 2015). The last but not the least, various factors may affect the quantification of strains, including vendors, algorithms used, sequence and parameters of image acquisition, and even software versions. The reference values provided by our study are software and algorithms specific, they can't be simply applied under other circumstances.

5 Summary

Cardiovascular magnetic resonance based tissue tracking (CMR-TT) provides comprehensive, dynamic and time-saving assessment of left- and right-ventricular (LV and RV) global, regional and segmental strains. In this study, we provided detailed insight into the feasibility, reproducibility and reference values of biventricular global and segmental strains using two- and three-dimensional (2/3D) CMR-TT in a large healthy population.

The 3D tracking mode of CMR-TT took the out-of-plane motion of myocardium into consideration, and constructed a 3D model to increase the tracking ability at all segments, especially in LV basal part. The intra-observer reproducibility of 3D global systolic peak strains in all directions ranged from 2.26% to 5.96%, which were acceptable. By comparison, the intra-observer variability of 3D global systolic mean strain maximizes for radial measurement, it resulted as 21.25%. The above findings suggested us that LV 3D global systolic peak strains could be an efficient parameter to describe the myocardial deformation.

RV longitudinal shortening is the most important motivation of RV deformation. Considering the RV free wall (RVFW) avoids the passive influence from the interventricular septum, only RVFW longitudinal strain (LS) was analyzed in this study.

Demographic, morphological and functional parameters of participants differ between males and females, and between the elderly and young subjects. According to the correlation analysis, LV strains were positively correlated with LV ejection fraction and negatively correlated with LV end-diastolic and end-systolic volume index. And these parameters are different between age and gender subgroups. Therefore, we analyzed the gender- and age-

related difference of biventricular global strains in subgroups. Finally, we drew the conclusions: i) females and the elderly subjects presented larger magnitude of LV global peak strains than males and young population; ii) females shown more negative RVFW-LS than males, age-related difference wasn't revealed.

Considering the different thickness of myocardium and local architecture of ventricles, the base-to-apex gradient was discussed for both LV and RV myocardium. We demonstrated that: i) the LV basal part presented greater deformation than the apical part in all of radial, circumferential and longitudinal directions, which was confirmed by both of 2D and 3D CMR-TT; ii) the longitudinal deformation of RV base is stronger than that of apex.

In conclusion, due to the good feasibility and reproducibility, we believe that CMR-TT is a practical and valuable modality in evaluating biventricular global and segmental movement. Considering the algorithms used by CMR-TT and the characteristics of humans, it's necessary to propose the establishment and application of specific reference values for separate modalities and groups in clinical routine.

6 Reference

1. Abraham, T.P., Dimaano, V.L., and Liang, H.Y. Role of tissue Doppler and strain echocardiography in current clinical practice. Circulation *116*, 2597-2609 (2007).
2. American College of Cardiology Foundation Task Force on Expert Consensus, D., Hundley, W.G., Bluemke, D.A., Finn, J.P., Flamm, S.D., Fogel, M.A., Friedrich, M.G., Ho, V.B., Jerosch-Herold, M., Kramer, C.M.*, et al.* ACCF/ACR/AHA/NASCI/SCMR 2010 expert consensus document on cardiovascular magnetic resonance: a report of the American College of Cardiology Foundation Task Force on Expert Consensus Documents. J Am Coll Cardiol *55*, 2614-2662 (2010).
3. Amzulescu, M.S., De Craene, M., Langet, H., Pasquet, A., Vancraeynest, D., Pouleur, A.C., Vanoverschelde, J.L., and Gerber, B.L. Myocardial strain imaging: review of general principles, validation, and sources of discrepancies. Eur Heart J Cardiovasc Imaging *20*, 605-619 (2019).
4. Andre, F., Steen, H., Matheis, P., Westkott, M., Breuninger, K., Sander, Y., Kammerer, R., Galuschky, C., Giannitsis, E., Korosoglou, G.*, et al.* Age- and gender-related normal left ventricular deformation assessed by cardiovascular magnetic resonance feature tracking. J Cardiovasc Magn R *17* (2015).
5. Antoni, M.L., Mollema, S.A., Delgado, V., Atary, J.Z., Borleffs, C.J.W., Boersma, E., Holman, E.R., van der Wall, E.E., Schalij, M.J., and Bax, J.J. Prognostic importance of strain and strain rate after acute myocardial infarction. European Heart Journal *31*, 1640-1647 (2010).
6. Axel, L., and Dougherty, L. Heart wall motion: improved method of spatial modulation of magnetization for MR imaging. Radiology *172*, 349-350 (1989).
7. Ballester-Rodes, M., Flotats, A., Torrent-Guasp, F., Ballester-Alomar, M., Carreras, F., Ferreira, A., and Narula, J. Base-to-apex ventricular activation: Fourier studies in 29 normal individuals. Eur J Nucl Med Mol Imaging *32*, 1481-1483 (2005).
8. Barreiro-Perez, M., Curione, D., Symons, R., Claus, P., Voigt, J.U., and Bogaert, J. Left ventricular global myocardial strain assessment comparing the reproducibility of four commercially available CMR-feature tracking algorithms. Eur Radiol *28*, 5137-5147 (2018).
9. Berganza, F.M., de Alba, C.G., Ozcelik, N., and Adebo, D. Cardiac Magnetic Resonance

Feature Tracking Biventricular Two-Dimensional and Three-Dimensional Strains to Evaluate Ventricular Function in Children After Repaired Tetralogy of Fallot as Compared with Healthy Children. Pediatric Cardiology *38*, 566-574 (2017).

10. Bogaert, J., and Rademakers, F.E. Regional nonuniformity of normal adult human left ventricle. Am J Physiol Heart Circ Physiol *280*, H610-620 (2001).
11. Cao, J.J., Ngai, N., Duncanson, L., Cheng, J., Gliganic, K., and Chen, Q.Z. A comparison of both DENSE and feature tracking techniques with tagging for the cardiovascular magnetic resonance assessment of myocardial strain. J Cardiovasc Magn R *20* (2018).
12. Carlsson, M., Ugander, M., Heiberg, E., and Arheden, H. The quantitative relationship between longitudinal and radial function in left, right, and total heart pumping in humans. Am J Physiol-Heart C *293*, H636-H644 (2007).
13. Cerqueira, M.D., Weissman, N.J., Dilsizian, V., Jacobs, A.K., Kaul, S., Laskey, W.K., Pennell, D.J., Rumberger, J.A., Ryan, T., Verani, M.S.*, et al.* Standardized myocardial segmentation and nomenclature for tomographic imaging of the heart. A statement for healthcare professionals from the Cardiac Imaging Committee of the Council on Clinical Cardiology of the American Heart Association. Int J Cardiovasc Imaging *18*, 539-542 (2002).
14. Chang, W.T., Tsai, W.C., Liu, Y.W., Lee, C.H., Liu, P.Y., Chen, J.Y., Li, Y.H., and Tsai, L.M. Changes in right ventricular free wall strain in patients with coronary artery disease involving the right coronary artery. J Am Soc Echocardiogr *27*, 230-238 (2014).
15. Cheng, S., Fernandes, V.R.S., Bluemke, D.A., McClelland, R.L., Kronmal, R.A., and Lima, J.A.C. Age-Related Left Ventricular Remodeling and Associated Risk for Cardiovascular Outcomes The Multi-Ethnic Study of Atherosclerosis. Circ-Cardiovasc Imag *2*, 191-198 (2009).
16. Chia, E.M., Hsieh, C.H.C., Boyd, A., Pham, P., Vidaic, J., Leung, D., and Thomas, L. Effects of Age and Gender on Right Ventricular Systolic and Diastolic Function Using Two-Dimensional Speckle-Tracking Strain. Journal of the American Society of Echocardiography *27*, 1079-U1175 (2014).
17. Claus, P., Omar, A.M.S., Pedrizzetti, G., Sengupta, P.P., and Nagel, E. Tissue Tracking Technology for Assessing Cardiac Mechanics: Principles, Normal Values, and Clinical Applications. JACC Cardiovasc Imaging *8*, 1444-1460 (2015).

18. de Siqueira, M.E.M., Pozo, E., Fernandes, V.R., Sengupta, P.P., Modesto, K., Gupta, S.S., Barbeito-Caamano, C., Narula, J., Fuster, V., Caixeta, A.*, et al.* Characterization and clinical significance of right ventricular mechanics in pulmonary hypertension evaluated with cardiovascular magnetic resonance feature tracking. J Cardiovasc Magn R *18* (2016).
19. Diao, K.Y., Yang, Z.G., Ma, M., He, Y., Zhao, Q., Liu, X., Gao, Y., Xie, L.J., and Guo, Y.K. The Diagnostic Value of Global Longitudinal Strain (GLS) on Myocardial Infarction Size by Echocardiography: A Systematic Review and Meta-analysis. Sci Rep-Uk *7* (2017).
20. Ferreira, R.G., Worthington, A., Huang, C.C., Aranki, S.F., and Muehlschlegel, J.D. Sex Differences in the Prevalence of Diastolic Dysfunction in Cardiac Surgical Patients. J Cardiac Surg *30*, 238-245 (2015).
21. Fischer, S.E., McKinnon, G.C., Maier, S.E., and Boesiger, P. Improved myocardial tagging contrast. Magn Reson Med *30*, 191-200 (1993).
22. Focardi, M., Cameli, M., Carbone, S.F., Massoni, A., De Vito, R., Lisi, M., and Mondillo, S. Traditional and innovative echocardiographic parameters for the analysis of right ventricular performance in comparison with cardiac magnetic resonance. Eur Heart J Cardiovasc Imaging *16*, 47-52 (2015).
23. Haddad, F., Doyle, R., Murphy, D.J., and Hunt, S.A. Right ventricular function in cardiovascular disease, part II: pathophysiology, clinical importance, and management of right ventricular failure. Circulation *117*, 1717-1731 (2008a).
24. Haddad, F., Hunt, S.A., Rosenthal, D.N., and Murphy, D.J. Right ventricular function in cardiovascular disease, part I: Anatomy, physiology, aging, and functional assessment of the right ventricle. Circulation *117*, 1436-1448 (2008b).
25. Hamada-Harimura, Y., Seo, Y., Ishizu, T., Nishi, I., Machino-Ohtsuka, T., Yamamoto, M., Sugano, A., Sato, K., Sai, S., Obara, K.*, et al.* Incremental Prognostic Value of Right Ventricular Strain in Patients With Acute Decompensated Heart Failure. Circ Cardiovasc Imaging *11*, e007249 (2018).
26. Hardegree, E.L., Sachdev, A., Villarraga, H.R., Frantz, R.P., McGoon, M.D., Kushwaha, S.S., Hsiao, J.F., McCully, R.B., Oh, J.K., Pellikka, P.A.*, et al.* Role of Serial Quantitative Assessment of Right Ventricular Function by Strain in Pulmonary Arterial Hypertension. American Journal of Cardiology *111*, 143-148 (2013).

27. Hor, K.N., Baumann, R., Pedrizzetti, G., Tonti, G., Gottliebson, W.M., Taylor, M., Benson, D.W., and Mazur, W. Magnetic Resonance Derived Myocardial Strain Assessment Using Feature Tracking. Jove-J Vis Exp (2011).
28. Hung, C.L., Goncalves, A., Shah, A.M., Cheng, S., Kitzman, D., and Solomon, S.D. Age- and Sex-Related Influences on Left Ventricular Mechanics in Elderly Individuals Free of Prevalent Heart Failure: The ARIC Study (Atherosclerosis Risk in Communities). Circ-Cardiovasc Imag *10* (2017).
29. Jiang, K., and Yu, X. Quantification of regional myocardial wall motion by cardiovascular magnetic resonance. Quant Imaging Med Surg *4*, 345-357 (2014).
30. Kawakubo, M., Nagao, M., Kumazawa, S., Yamasaki, Y., Chishaki, A.S., Nakamura, Y., Honda, H., and Morishita, J. Evaluation of ventricular dysfunction using semi-automatic longitudinal strain analysis of four-chamber cine MR imaging. Int J Cardiovasc Imaging *32*, 283-289 (2016).
31. Kemal, H.S., Kayikcioglu, M., Kultursay, H., Vuran, O., Nalbantgil, S., Mogulkoc, N., and Can, L. Right ventricular free-wall longitudinal speckle tracking strain in patients with pulmonary arterial hypertension under specific treatment. Echocardiogr-J Card *34*, 530-536 (2017).
32. Klinke, V., Muzzarelli, S., Lauriers, N., Locca, D., Vincenti, G., Monney, P., Lu, C., Nothnagel, D., Pilz, G., Lombardi, M.*, et al.* Quality assessment of cardiovascular magnetic resonance in the setting of the European CMR registry: description and validation of standardized criteria. J Cardiovasc Magn Reson *15*, 55 (2013).
33. Kocica, M.J., Corno, A.F., Carreras-Costa, F., Ballester-Rodes, M., Moghbel, M.C., Cueva, C.N.C., Lackovic, V., Kanjuh, V.I., and Torrent-Guasp, F. The helical ventricular myocardial band: global, three-dimensional, functional architecture of the ventricular myocardium. Eur J Cardio-Thorac *29*, S21-S40 (2006).
34. Kocica, M.J., Corno, A.F., Lackovic, V., and Kanjuh, V.I. The helical ventricular myocardial band of Torrent-Guasp. Semin Thorac Cardiovasc Surg Pediatr Card Surg Annu, 52-60 (2007).
35. Lamacie, M.M., Thavendiranathan, P., Hanneman, K., Greiser, A., Jolly, M.P., Ward, R., and Wintersperger, B.J. Quantification of global myocardial function by cine MRI deformable registration-based analysis: Comparison with MR feature tracking and speckle-tracking echocardiography. Eur Radiol *27*, 1404-1415 (2017).

36. Lee, K., Kwon, O., Lee, E.J., Sin, M.J., Lee, J.S., Lee, S., Kang, D.H., Song, J.K., and Song, J.M. Prognostic value of echocardiographic parameters for right ventricular function in patients with acute non-massive pulmonary embolism. Heart Vessels *34*, 1187-1195 (2019).
37. Levy, P.T., Mejia, A.A.S., Machefsky, A., Fowler, S., Holland, M.R., and Singh, G.K. Normal Ranges of Right Ventricular Systolic and Diastolic Strain Measures in Children: A Systematic Review and Meta-Analysis. Journal of the American Society of Echocardiography *27*, 549-U145 (2014).
38. Liu, B., Dardeer, A.M., Moody, W.E., Edwards, N.C., Hudsmith, L.E., and Steeds, R.P. Reference ranges and reproducibility studies for right heart myocardial deformation by feature tracking cardiovascular magnetic resonance imaging. Data Brief *16*, 244-249 (2018a).
39. Liu, B.Y., Dardeer, A.M., Moody, W.E., Edwards, N.C., Hudsmith, L.E., and Steeds, R.P. Normal values for myocardial deformation within the right heart measured by feature-tracking cardiovascular magnetic resonance imaging. International Journal of Cardiology *252*, 220-223 (2018b).
40. Liu, B.Y., Dardeer, A.M., Moody, W.E., Hayer, M.K., Baig, S., Price, A.M., Leyva, F., Edwards, N.C., and Steeds, R.P. Reference ranges for three-dimensional feature tracking cardiac magnetic resonance: comparison with two-dimensional methodology and relevance of age and gender. Int J Cardiovas Imag *34*, 761-775 (2018c).
41. Lu, J.C., Balasubramanian, S., Yu, S., Mahani, M.G., Agarwal, P.P., and Dorfman, A.L. Reproducibility and Agreement of Tissue Tracking versus Feature Tracking for Strain Measurement on Cardiac MR Images in Patients with Repaired Tetralogy of Fallot. Radiology: Cardiothoracic Imaging *1*, e180005 (2019).
42. Luetkens, J.A., Petry, P., Kuetting, D., Dabir, D., Schmeel, F.C., Homsi, R., Schild, H.H., and Thomas, D. Left and right ventricular strain in the course of acute myocarditis: a cardiovascular magnetic resonance study. Rofo-Fortschr Rontg *190*, 722-732 (2018).
43. Luis, S.A., Chan, J., and Pellikka, P.A. Echocardiographic Assessment of Left Ventricular Systolic Function: An Overview of Contemporary Techniques, Including Speckle-Tracking Echocardiography. Mayo Clin Proc *94*, 125-138 (2019).
44. Maceira, A.M., Tuset-Sanchis, L., Lopez-Garrido, M., San Andres, M., Lopez-Lereu, M.P., Monmeneu, J.V., Garcia-Gonzalez, M.P., and Higueras, L. Feasibility and

reproducibility of feature-tracking-based strain and strain rate measures of the left ventricle in different diseases and genders. Journal of Magnetic Resonance Imaging *47*, 1415-1425 (2018).

45. Mathur, S., Dreisbach, J.G., Karur, G.R., Iwanochko, R.M., Morel, C.F., Wasim, S., Nguyen, E.T., Wintersperger, B.J., and Hanneman, K. Loss of base-to-apex circumferential strain gradient assessed by cardiovascular magnetic resonance in Fabry disease: relationship to T1 mapping, late gadolinium enhancement and hypertrophy. J Cardiovasc Magn Reson *21*, 45 (2019).
46. Meris, A., Faletra, F., Conca, C., Klersy, C., Regoli, F., Klimusina, J., Penco, M., Pasotti, E., Pedrazzini, G.B., Moccetti, T.*, et al.* Timing and magnitude of regional right ventricular function: a speckle tracking-derived strain study of normal subjects and patients with right ventricular dysfunction. J Am Soc Echocardiogr *23*, 823-831 (2010).
47. Mirea, O., Berceanu, M., Donoiu, I., Militaru, C., Saftoiu, A., and Istratoaie, O. Variability of right ventricular global and segmental longitudinal strain measurements. Echocardiogr-J Card *36*, 102-109 (2019).
48. Mitchell, F.M., Prasad, S.K., Greil, G.F., Drivas, P., Vassiliou, V.S., and Raphael, C.E. Cardiovascular magnetic resonance: Diagnostic utility and specific considerations in the pediatric population. World J Clin Pediatr *5*, 1-15 (2016).
49. Mochizuki, A., Yuda, S., Oi, Y., Kawamukai, M., Nishida, J., Kouzu, H., Muranaka, A., Kokubu, N., Shimoshige, S., Hashimoto, A.*, et al.* Assessment of left atrial deformation and synchrony by three-dimensional speckle-tracking echocardiography: comparative studies in healthy subjects and patients with atrial fibrillation. J Am Soc Echocardiogr *26*, 165-174 (2013).
50. Mouton, S., Ridon, H., Fertin, M., Pentiah, A.D., Goemine, C., Petyt, G., Lamblin, N., Coisne, A., Foucher-Hossein, C., Montaigne, D.*, et al.* 2D-speckle tracking right ventricular strain to assess right ventricular systolic function in systolic heart failure. Analysis of the right ventricular free and posterolateral walls. Int J Cardiol *245*, 190-195 (2017).
51. Muraru, D., Onciul, S., Peluso, D., Soriani, N., Cucchini, U., Aruta, P., Romeo, G., Cavalli, G., Iliceto, S., and Badano, L.P. Sex- and Method-Specific Reference Values for Right Ventricular Strain by 2-Dimensional Speckle-Tracking Echocardiography. Circ Cardiovasc Imaging *9*, e003866 (2016).

52. Nucifora, G., Miller, J., Gillebert, C., Shah, R., Perry, R., Raven, C., Joseph, M.X., and Selvanayagam, J.B. Ascending Aorta and Myocardial Mechanics in Patients with "Clinically Normal" Bicuspid Aortic Valve Insights from Cardiovascular Magnetic Resonance Tissue-Tracking Imaging. Int Heart J *59*, 741-749 (2018).
53. Okura, H., Takada, Y., Yamabe, A., Kubo, T., Asawa, K., Ozaki, T., Yamagishi, H., Toda, I., Yoshiyama, M., Yoshikawa, J.*, et al.* Age- and Gender-Specific Changes in the Left Ventricular Relaxation A Doppler Echocardiographic Study in Healthy Individuals. Circ-Cardiovasc Imag *2*, 41-46 (2009).
54. Omar, A.M., Vallabhajosyula, S., and Sengupta, P.P. Left ventricular twist and torsion: research observations and clinical applications. Circ Cardiovasc Imaging *8* (2015).
55. Opdahl, A., Helle-Valle, T., Skulstad, H., and Smiseth, O.A. Strain, strain rate, torsion, and twist: echocardiographic evaluation. Curr Cardiol Rep *17*, 568 (2015).
56. Park JH, Negishi K, Kwon DH, Popovic ZB, Grimm RA, and Marwick TH. Validation of Global Longitudinal Strain and Strain Rate as Reliable Markers of Right Ventricular Dysfunction: Comparison with Cardiac Magnetic Resonance and Outcome. J Cardiovasc Ultrasound *22*, 113–120 (2014).
57. Pedrizzetti, G., Claus, P., Kilner, P.J., and Nagel, E. Principles of cardiovascular magnetic resonance feature tracking and echocardiographic speckle tracking for informed clinical use. J Cardiovasc Magn R *18* (2016).
58. Pellerin, D., Sharma, R., Elliott, P., and Veyrat, C. Tissue Doppler, strain, and strain rate echocardiography for the assessment of left and right systolic ventricular function. Heart *89*, 9-17 (2003).
59. Pennell, D.J., Sechtem, U.P., Higgins, C.B., Manning, W.J., Pohost, G.M., Rademakers, F.E., van Rossum, A.C., Shaw, L.J., Yucel, E.K., Society for Cardiovascular Magnetic, R.*, et al.* Clinical indications for cardiovascular magnetic resonance (CMR): Consensus Panel report. Eur Heart J *25*, 1940-1965 (2004).
60. Petersen, S.E., Aung, N., Sanghvi, M.M., Zemrak, F., Fung, K., Paiva, J.M., Francis, J.M., Khanji, M.Y., Lukaschuk, E., Lee, A.M.*, et al.* Reference ranges for cardiac structure and function using cardiovascular magnetic resonance (CMR) in Caucasians from the UK Biobank population cohort. J Cardiovasc Magn R *19* (2017).
61. Pislaru, C., and Pellikka, P.A. Tissue Doppler and strain-rate imaging in cardiac ultrasound imaging: valuable tools or expensive ornaments? Expert Rev Cardiovasc

Ther *3*, 1-4 (2005).

62. Plewes, D.B., and Kucharczyk, W. Physics of MRI: a primer. J Magn Reson Imaging *35*, 1038-1054 (2012).
63. Prasad, S.K., and Lota, A.S. Right Ventricle Dysfunction in Cardiomyopathy: To Measure Is to Know. JACC Cardiovasc Imaging *10*, 1237-1239 (2017).
64. Qu, Y.Y., Li, H., Rottbauer, W., Ma, G.S., Buckert, D., and Rasche, V. Right ventricular free wall longitudinal strain and strain rate quantification with cardiovascular magnetic resonance based tissue tracking. Int J Cardiovasc Imaging *36*, 1985-1996 (2020).
65. Qu, Y.Y., Paul, J., Li, H., Ma, G.S., Buckert, D., and Rasche, V. Left ventricular myocardial strain quantification with two- and three-dimensional cardiovascular magnetic resonance based tissue tracking. Quant Imaging Med Surg *11*, 1421-1436 (2021).
66. Ridgway, J.P. Cardiovascular magnetic resonance physics for clinicians: part I. J Cardiovasc Magn Reson *12*, 71 (2010).
67. Riffel, J.H., Andre, F., Maertens, M., Rost, F., Keller, M.G.P., Giusca, S., Seitz, S., Kristen, A.V., Muller, M., Giannitsis, E.*, et al.* Fast assessment of long axis strain with standard cardiovascular magnetic resonance: a validation study of a novel parameter with reference values. J Cardiovasc Magn R *17* (2015).
68. Rimbas, R.C., Mihaila, S., Enescu, O.A., and Vinereanu, D. A new comprehensive 12-segment approach to right ventricular systolic and diastolic functions by 2D speckle tracking echocardiography in healthy individuals. Echocardiogr-J Card *33*, 1866-1873 (2016).
69. Romano, S., Romer, B., Evans, K., Trybula, M., Shenoy, C., Kwong, R.Y., and Farzaneh-Far, A. Prognostic Implications of Blunted Feature-Tracking Global Longitudinal Strain During Vasodilator Cardiovascular Magnetic Resonance Stress Imaging. JACC Cardiovasc Imaging (2019).
70. Rong, L.Q., Yum, B., Abouzeid, C., Palumbo, M.C., Brouwer, L.R., Devereux, R.B., Girardi, L.N., Weinsaft, J.W., Gaudino, M., and Kim, J. Echocardiographic predictors of intraoperative right ventricular dysfunction: a 2D and speckle tracking echocardiography study. Cardiovasc Ultrasound *17*, 11 (2019).
71. Sabe, M.A., Sabe, S.A., Kusunose, K., Flamm, S.D., Griffin, B.P., and Kwon, D.H. Predictors and Prognostic Significance of Right Ventricular Ejection Fraction in Patients

With Ischemic Cardiomyopathy. Circulation *134*, 656-665 (2016).

72. Salehi Ravesh, M., Rickers, C., Bannert, F.J., Hautemann, D., Al Bulushi, A., Gabbert, D.D., Wegner, P., Kis, E., Hansen, J.H., Jerosch-Herold, M.*, et al.* Longitudinal Deformation of the Right Ventricle in Hypoplastic Left Heart Syndrome: A Comparative Study of 2D-Feature Tracking Magnetic Resonance Imaging and 2D-Speckle Tracking Echocardiography. Pediatr Cardiol *39*, 1265-1275 (2018).
73. Sanz, J., Sanchez-Quintana, D., Bossone, E., Bogaard, H.J., and Naeije, R. Anatomy, Function, and Dysfunction of the Right Ventricle: JACC State-of-the-Art Review. J Am Coll Cardiol *73*, 1463-1482 (2019).
74. Sanz-de la Garza M, Giraldeau G, Marin J, Imre Sarvari S, Guasch E, Gabrielli L, Brambila C, Bijnens B, and Sitges M. Should the septum be included in the assessment of right ventricular longitudinal strain? An ultrasound two-dimensional speckle-tracking stress study. Int J Cardiovasc Imaging *[Epub ahead of print]* (2019).
75. Scatteia, A., Baritussio, A., and Bucciarelli-Ducci, C. Strain imaging using cardiac magnetic resonance. Heart Failure Reviews *22*, 465-476 (2017).
76. Schulz-Menger, J., Bluemke, D.A., Bremerich, J., Flamm, S.D., Fogel, M.A., Friedrich, M.G., Kim, R.J., von Knobelsdorff-Brenkenhoff, F., Kramer, C.M., Pennell, D.J.*, et al.* Standardized image interpretation and post processing in cardiovascular magnetic resonance: Society for Cardiovascular Magnetic Resonance (SCMR) board of trustees task force on standardized post processing. J Cardiovasc Magn Reson *15*, 35 (2013).
77. Schuster, A., Stahnke, V.C., Unterberg-Buchwald, C., Kowallick, J.T., Lamata, P., Steinmetz, M., Kutty, S., Fasshauer, M., Staab, W., Sohns, J.M.*, et al.* Cardiovascular magnetic resonance feature-tracking assessment of myocardial mechanics: Intervendor agreement and considerations regarding reproducibility. Clin Radiol *70*, 989-998 (2015).
78. Sengupta, P.P., Korinek, J., Belohlavek, M., Narula, J., Vannan, M.A., Jahangir, A., and Khandheria, B.K. Left ventricular structure and function: basic science for cardiac imaging. J Am Coll Cardiol *48*, 1988-2001 (2006).
79. Streeter, D.D., Jr., Spotnitz, H.M., Patel, D.P., Ross, J., Jr., and Sonnenblick, E.H. Fiber orientation in the canine left ventricle during diastole and systole. Circ Res *24*, 339-347 (1969).
80. Suever, J.D., Wehner, G.J., Jing, L.Y., Powell, D.K., Hamlet, S.M., Grabau, J.D., Mojsejenko, D., Andres, K.N., Haggerty, C.M., and Fornwalt, B.K. Right Ventricular

Strain, Torsion, and Dyssynchrony in Healthy Subjects Using 3D Spiral Cine DENSE Magnetic Resonance Imaging. Ieee T Med Imaging *36*, 1076-1085 (2017).

81. Taylor, R.J., Moody, W.E., Umar, F., Edwards, N.C., Taylor, T.J., Stegemann, B., Townend, J.N., Hor, K.N., Steeds, R.P., Mazur, W.*, et al.* Myocardial strain measurement with feature-tracking cardiovascular magnetic resonance: normal values. Eur Heart J Cardiovasc Imaging *16*, 871-881 (2015).
82. Torrent-Guasp, F., Ballester, M., Buckberg, G.D., Carreras, F., Flotats, A., Carrio, I., Ferreira, A., Samuels, L.E., and Narula, J. Spatial orientation of the ventricular muscle band: Physiologic contribution and surgical implications. J Thorac Cardiov Sur *122*, 389-392 (2001).
83. Truong, V.T., Safdar, K.S., Kalra, D.K., Gao, X., Ambach, S., Taylor, M.D., Moore, R., Taylor, R.J., Germann, J., Toro-Salazar, O.*, et al.* Cardiac magnetic resonance tissue tracking in right ventricle: Feasibility and normal values. Magn Reson Imaging *38*, 189-195 (2017).
84. Voelkel, N.F., Quaife, R.A., Leinwand, L.A., Barst, R.J., McGoon, M.D., Meldrum, D.R., Dupuis, J., Long, C.S., Rubin, L.J., Smart, F.W.*, et al.* Right ventricular function and failure: report of a National Heart, Lung, and Blood Institute working group on cellular and molecular mechanisms of right heart failure. Circulation *114*, 1883-1891 (2006).
85. von Knobelsdorff-Brenkenhoff, F., and Schulz-Menger, J. Role of cardiovascular magnetic resonance in the guidelines of the European Society of Cardiology. J Cardiovasc Magn Reson *18*, 6 (2016).
86. Wang, H., and Amini, A.A. Cardiac motion and deformation recovery from MRI: a review. IEEE Trans Med Imaging *31*, 487-503 (2012).
87. Wazen, R.M., Currey, J.A., Guo, H.Q., Brunski, J.B., Helms, J.A., and Nanci, A. Micromotion-induced strain fields influence early stages of repair at bone-implant interfaces. Acta Biomaterialia *9*, 6663-6674 (2013).
88. Weidemann, F., Wacker, C., Rauch, A., Bauer, W.R., Bijnens, B., Sutherland, G.R., Ertl, G., Voelker, W., Fidler, F., and Strotmann, J.M. Sequential changes of myocardial function during acute myocardial infarction, in the early and chronic phase after coronary intervention described by ultrasonic strain rate imaging. Journal of the American Society of Echocardiography *19*, 839-847 (2006).

89. Yingchoncharoen, T., Agarwal, S., Popovic, Z.B., and Marwick, T.H. Normal ranges of left ventricular strain: a meta-analysis. J Am Soc Echocardiogr *26*, 185-191 (2013).
90. Zerhouni, E.A., Parish, D.M., Rogers, W.J., Yang, A., and Shapiro, E.P. Human heart: tagging with MR imaging--a method for noninvasive assessment of myocardial motion. Radiology *169*, 59-63 (1988).
91. Zou, H., Xi, C., Zhao, X.D., Koh, A.S., Gao, F., Su, Y., Tan, R.S., Allen, J., Lee, L.C., Genet, M.*, et al.* Quantification of Biventricular Strains in Heart Failure With Preserved Ejection Fraction Patient Using Hyperelastic Warping Method. Front Physiol *9* (2018).

7 Acknowledgement

The acknowledgment has been removed due to data privacy protection.

8 Curriculum vitae

Personal Information

Name: Yangyang

Surname: Qu

Gender: Female

Birth date: 1991

Education

11/2016 – present Experimental Cardiovascular Imaging, Ulm University, Ulm, Germany

Dr.Med. candidate, focusing on biventricular strains

09/2014 – 06/2017 Medical School of Southeast University, Nanjing, P. R. China

Master degree, majoring in internal medicine

09/2009 – 07/2014 Medical School of Southeast University, Nanjing, P. R. China

Bachelor degree, majoring in clinical medicine

Publication

1. **Yang-Yang Qu**, Dominik Buckert, Gen-shan Ma, Volker Rasche. Quantitative Assessment of Left and Right Atrial Strains Using Cardiovascular Magnetic Resonance Based Tissue Tracking. *Frontier in Cardiovascular Medicine*. 2021 Jun 24;8:690240.
2. **Yang-Yang Qu**, Jan Paul, Hao Li, Gen-Shan Ma, Dominik Buckert, Volker Rasche. Left ventricular myocardial strain quantification with two- and three-dimensional cardiovascular magnetic resonance based tissue tracking. *Quantitative Imaging in Medicine and Surgery*. 2021 Apr;11(4):1421-1436.
3. **Yang-Yang Qu,** Hao Li, Wolfgang Rottbauer, Gen-Shan Ma, Dominik Buckert, Volker Rasche. Right ventricular free wall longitudinal strain and strain rate quantification with cardiovascular

magnetic resonance based tissue tracking. *International Journal of Cardiovascular Imaging. 2020* Oct;36(10):1985-1996.

4. Dominik Buckert, Raid Tibi, Maciej Cieslik, Michael Radermacher, **Yang-Yang Qu**, Volker Rasche, Peter Bernhardt, Vinzenz Hombach, Wolfgang Rottbauer, Jochen Wöhrle. Myocardial strain characteristics and outcomes after transcatheter aortic valve replacement. *Cardiology Journal*. 2017 Oct 24. Epub 2017 Oct 24.

Abstract

1. **Yang-Yang Qu**, Dominik Buckert, Gen-shan Ma, Volker Rasche. Biventricular global and regional strain measured by cardiovascular magnetic resonance based tissue tracking. ESC 2019. Paris, France. 2019.08.31-09.04 (Oral presentation)
2. **Yang-yang Qu**, Jan Paul, Dominik Buckert, Gen-shan Ma, Volker Rasche. Right-ventricular longitudinal strain reference values of healthy volunteers by age and gender as measured with CMR tissue tracking. 26th International Society for Magnetic Resonance in Medicine (ISMRM). Paris, France. 2018.06.16-21 (Poster)
3. **Yang-yang Qu**, Jan Paul, Dominik Buckert, Volker Rasche. Left-ventricular strain measured by 2D vs 3D tissue tracking requires separate normal values. CMR 2018. Barcelona, Spain. 2018.01.31-02.03 (Poster)
4. **Yang-yang Qu**, Jan Paul, Dominik Buckert, Volker Rasche. Left-ventricular strain reference values of healthy volunteers by age and gender as measured with 3D tissue tracking. CMR 2018. Barcelona, Spain. 2018.01.31-02.03 (Poster)
5. Jan Paul, **Yang-yang Qu**, Volker Rasche. 3D stack-of-stars cardiac cine MRI: Free-breathing vs. respiratory gated reconstruction, 25th ISMRM annual meeting & exhibition, Honolulu, Hawai'i, America. 2017.04.22-27 (Poster)